Instability and transition in finite-amplitude Kelvin–Helmholtz and Holmboe waves

By W. D. SMYTH AND W. R. PELTIER

Department of Physics, University of Toronto, Toronto, Ontario, Canada, M5S 1A7

We investigate the transition to turbulence in a free shear layer which contains a thin central region of stable density stratification. The fluid is assumed to possess Prandtl number significantly larger than unity, and the flow may exhibit either Holmboe or Kelvin–Helmholtz (KH) instability, depending upon the intensity of the stratification. A sequence of two-dimensional nonlinear numerical simulations of flows near the KH–Holmboe transition (i.e. having bulk Richardson numbers near $\frac{1}{4}$) clearly illustrates the structural relationship between Holmboe and Kelvin–Helmholtz waves. The time-dependent nonlinear wave states delivered by the simulations are subjected to a three-dimensional normal-mode stability analysis in order to discover the physical processes that might drive the flow towards a turbulent state. Strong secondary instability is found to persist up to large spanwise wavenumbers, with no indication of a preferred lengthscale. These results indicate that secondary instability may lead the flow directly into the turbulent state.

1. Introduction

The transition to turbulence in a stably stratified flow is a process of central importance in geophysical fluid systems. The evolution of such flows is commonly studied in terms of a model problem in which the initial state is assumed to consist of a free shear layer, or mixing layer, in a fluid whose density varies in the vertical direction. In naturally occurring flows, density tends to decrease exponentially with height, a circumstance that is difficult to create in the laboratory, and one which involves theoretical complexities owing to the ability of the fluid to radiate energy away from the shear layer in the form of internal waves. These additional complexities are often bypassed by focusing consideration upon the case in which density varies only in a localized region surrounding the centre of the shear layer, a situation which is also common in geophysical flows. (The stratified layer is usually assumed to be located symmetrically with respect to the shear layer in order to avoid further complications due to asymmetry.) The influence of diffusion tends to drive such parallel flows towards a state in which the ratio of the depth of the shear layer to the depth of the stratified layer is equal to $Pr^{\frac{1}{2}}$, Pr being the Prandtl number (Smyth, Klaassen & Peltier 1988). In the Earth's atmosphere, $Pr \approx 1$, and those interested in atmospheric applications have thus tended to focus on the case in which the shear layer and the stratified layer have equal depths. These flows are linearly stable unless the minimum Richardson number is less than $\frac{1}{4}$, in which case the flow succumbs to Kelvin–Helmholtz (KH) instability (see Klaassen & Peltier 1985a, and references therein). In many geophysically relevant flows, however, the Prandtl number is significantly greater than unity. Thermally stratified water, for example, has $Pr \approx 7$, and salt-stratified water, as found in the oceans and which is employed

as the working fluid in most laboratory experiments on density-stratified flows, is characterized by Prandtl numbers of order 10^2. In these systems, we are more likely to see stratification confined primarily to a thin region surrounding the centre of the shear layer. This is the initial flow whose evolution we shall examine in the present paper.

Since the gradient Richardson number drops to zero away from the height of maximum shear in circumstances in which the stratified layer is sufficiently thin compared to the shear layer (e.g. Hazel 1972), this flow cannot usefully be characterized in terms of a minimum Richardson number, and one therefore employs in its place a bulk Richardson number Ri, which is equal to the value of the gradient Richardson number at the centre of the shear layer. When Ri is less than a critical value Ri_T, the flow is unstable to Kelvin–Helmholtz waves (Ri_T is equal to or somewhat greater than $\frac{1}{4}$), whereas when $Ri > Ri_T$ the flow exhibits Holmboe (or 'cusped') instability, an oscillatory disturbance having the appearance of a standing wave which periodically ejects plumes of stratified fluid away from the shear layer. In the inviscid limit, Holmboe instability persists up to arbitrarily large Ri. The linear stability of this initial state has been examined by Holmboe (1962), Hazel (1972), Nishida & Yoshida (1982) and Smyth & Peltier (1989, 1990). Experimental analyses of Holmboe waves have been carried out by Thorpe (1968), Browand & Wang (1972), Browand & Winant (1973), Yoshida (1977), Koop & Browand (1979) and Lawrence et al. (1987, 1990). Smyth et al. (1988) described the first finite-amplitude simulations of two-dimensional Holmboe waves using a standard, second-order accurate finite-difference model.

Since the seminal work of Ruelle & Takens (1971), it has become evident that an initially laminar flow may become turbulent via a finite sequence of distinct transitions corresponding to linear instabilities (as opposed to the earlier theory due to Landau, which required an infinite sequence of transitions). Cylindrical Couette flow (e.g. Di Prima & Swinney 1981) and Rayleigh–Bénard convection (e.g. Busse 1981) are examples of flows which have been found to evolve in accordance with this scenario as the value of an external forcing parameter is increased, and it seems likely that the time evolution of stratified shear layers may also be usefully examined in the context of this general paradigm, despite the absence of external forcing in models currently under investigation. Significant progress has been achieved in this direction for the case $Pr = 1$. Secondary instabilities in the form of convection rolls, knots, etc., introduce dependence upon the third spatial coordinate, which represents a crucial step on the route to turbulence, while pairing instabilities complicate the flow in two dimensions (see Klaassen & Peltier 1989, 1991; Collins & Maslowe 1988; or the review by Thorpe 1987b). Corresponding investigations have been carried out for the unstratified case (e.g. Pierrehumbert & Widnall 1982; Metcalfe et al. 1987).

Much less is known regarding the class of flows which exhibit Holmboe instability. One rather unique result, suggested by Browand & Wang (1972) and proved by Smyth & Peltier (1990), is that the initially one-dimensional flow may bifurcate directly into a three-dimensional state in a single transition (i.e. without the need for an intervening two-dimensional state). The laboratory experiments of Maxworthy & Browand (1975) reveal structures that are strongly suggestive of this three-dimensional Holmboe wave. However, this three-dimensional primary instability occurs only at small Reynolds numbers, where the flow is unlikely to develop strong turbulence, and over a restricted range of Ri. In general, the three-dimensional (and eventually turbulent) state must develop via secondary instability. Other laboratory investigations of Holmboe waves (Browand & Winant 1973; Koop 1976) have

revealed structures which are two-dimensional except for small, turbulent 'puffs' which appear on the plumes of the Holmboe wave. A theoretical explanation for these observations will be advanced in the present paper.

The research that we shall describe here has been undertaken with two main purposes in mind. Firstly, the work represents a continuation of our investigations into the rich phenomenology exhibited by flows occurring near the KH–Holmboe transition (see also Smyth *et al.* 1988; Smyth & Peltier 1989, 1990), and in this context we shall further examine the structural relationship between Holmboe and Kelvin–Helmholtz waves. Secondly, we shall investigate via two-dimensional non-separable linear stability analysis the secondary instabilities which induce three-dimensional motions in two-dimensional nonlinear Holmboe waves, and thus endeavour to explain the two distinct mechanisms for the introduction of three-dimensionality which have been observed in the laboratory experiments discussed above. These two goals are closely related. Since Holmboe waves become increasingly time-dependent as Ri becomes large ($Ri \gg Ri_T$), only in waves that develop near the KH–Holmboe transition can we expect the time-dependence of the two-dimensional flow to be sufficiently slow to permit a stability analysis in terms of normal modes.

In §2, we describe a sequence of two-dimensional nonlinear simulations of flows near $Ri = Ri_T$ which illustrate previously undiscovered aspects of the relationship between Kelvin–Helmholtz and Holmboe waves. In §3, we test the stability of these nonlinear waves to fully three-dimensional disturbances and elucidate in part the physical processes which must drive these flows towards the turbulent state. Section 4 contains a summary of our main conclusions.

2. Two-dimensional basic states

2.1. *Methodology*

In this subsection, we will describe in detail the numerical model that has been developed to simulate the evolution of two-dimensional nonlinear Kelvin–Helmholtz and Holmboe waves. For consistency with previous studies, we have assumed that the density stratification is thermal in origin and therefore have written the equations in terms of a potential temperature deviation. As the latter quantity is related to the potential density deviation by a simple change of sign, the results described here hold equally well for flows in which density stratification is otherwise produced.

The model equations are non-dimensionalized using a lengthscale h equal to the half-depth of the shear layer, a velocity scale V equal to half the total change in velocity across the shear layer, and a potential temperature deviation scale $R\delta$, in which R is the ratio of the depth of the shear layer to the depth of the stratified layer and δ is half the total potential temperature change across the flow. Non-dimensional parameters appearing in the model equations are the Reynolds number $Re = hV/\nu$, the Prandtl number $Pr = \nu/\kappa$, and the bulk Richardson number $Ri = gh\delta/V^2\Theta_0$. ν and κ are the diffusivities for momentum and heat, g is the gravitational acceleration and Θ_0 is the constant reference potential temperature from which the deviation θ is measured.

The two-dimensional waves that we shall examine here evolve from initial conditions of stably stratified shear flow for which the horizontal velocity and potential temperature deviations from the mean are given by:

$$u = \tanh(z - \tfrac{1}{2}H), \quad \theta = R^{-1}\tanh R(z - \tfrac{1}{2}H), \tag{1}$$

in which H is the height of the computational domain. As was demonstrated in Smyth *et al.* (1988), setting $R = Pr^{\frac{1}{2}}$ forces R to remain approximately constant as the background profiles diffuse. In the present study, our attention will be focused upon the representative case $R = 3$, $Pr = 9$. The Reynolds number will be fixed to the value $Re = 400$, and the bulk Richardson number Ri varied in order that we may examine the effects of changing ambient stratification upon the nonlinear waves as the KH–Holmboe transition is traversed. In addition to rendering the problem numerically tractable, the above choice of parameter values will allow us to closely approximate laboratory realizations of Kelvin–Helmholtz and Holmboe waves, as these waves are typically generated in flows with Reynolds numbers on the order of a few hundred.

Using the non-dimensionalization described above, the Boussinesq equations for a two-dimensional, thermally-stratified flow may be written as:

$$\omega_t = \partial(\omega, \psi) + Ri\theta_x + Re^{-1}\nabla^2\omega, \tag{2a}$$

$$\theta_t = \partial(\theta, \psi) + (RePr)^{-1}\nabla^2\theta, \tag{2b}$$

$$\omega = \nabla^2\psi, \tag{2c}$$

in which ω and ψ are the spanwise vorticity and the streamfunction, θ is the potential temperature, x and z are the streamwise and vertical coordinates, and t is the time. Subscripts denote partial derivatives, $\partial(a, b) \equiv a_x b_z - a_z b_x$ is the Jacobian operator and ∇^2 represents the two-dimensional Laplacian $\partial_{xx} + \partial_{zz}$. The streamfunction is defined by $u = -\psi_z$ and $w = \psi_x$, in which u and w are the streamwise and vertical velocity components, respectively.

At the upper and lower boundaries ($z = 0$ and $z = H$) of the computational domain, we impose free-slip, isothermal boundary conditions:

$$\omega = \psi = 0, \quad \theta_t = 0. \tag{3}$$

We seek solutions of (2) which are periodic in the streamwise direction, having wavelength L and fundamental wavenumber $\alpha = 2\pi/L$. Accordingly, we assume that the dependent fields may be written in the form

$$f(x, z, t) = \sum_{\nu=-N}^{N} f_\nu(z, t) e^{i\nu\alpha x}, \tag{4}$$

in which f may represent ω, ψ or θ. Note that $f_{-\nu} = f_\nu^*$, since $f(x, z, t)$ must be real. Because of this, we need only compute f_ν for $\nu = 0, 1, 2, \ldots, N$.

Substituting (4) into (2) and applying the usual Galerkin formalism, we obtain the following set of PDEs for the coefficient functions $\omega_\nu(z, t)$, $\psi_\nu(z, t)$ and $\theta_\nu(z, t)$; $\nu = -N, N$:

$$\frac{\partial\omega_\nu}{\partial t} = i\alpha \sum_{\lambda=\lambda_-}^{\lambda_+} (\nu - \lambda)\left(\frac{\partial\omega_\lambda}{\partial z}\omega_{\nu-\lambda} - \psi_{\nu-\lambda}\frac{\partial\omega_\lambda}{\partial z}\right) + i\alpha\nu Ri\theta_\nu + Re^{-1}\left(\frac{\partial^2\omega_\nu}{\partial z^2} - \nu^2\alpha^2\omega_\nu\right), \tag{5a}$$

$$\frac{\partial\theta_\nu}{\partial t} = i\alpha \sum_{\lambda=\lambda_-}^{\lambda_+} (\nu - \lambda)\left(\frac{\partial\psi_\lambda}{\partial z}\theta_{\nu-\lambda} - \psi_{\nu-\lambda}\frac{\partial\theta_\lambda}{\partial z}\right) + (RePr)^{-1}\left(\frac{\partial^2\theta_\nu}{\partial z^2} - \nu^2\alpha^2\theta_\nu\right), \tag{5b}$$

$$\omega_\nu = \frac{\partial^2\psi_\nu}{\partial z^2} - \nu^2\alpha^2\psi_\nu, \tag{5c}$$

in which $\lambda_- = \max(\nu - N, -N)$ and $\lambda_+ = \min(\nu + N, N)$. The z-dependence in these equations is now cast into finite-difference form by replacing z with a discrete variable z_μ, $\mu = 1, 2, \dots, M$, replacing the coefficient functions $f_\nu(z)$ with $f_{\mu\nu} = f_\nu(z_\mu)$ and replacing vertical derivatives with their second-order finite difference equivalents, viz.:

$$\frac{\partial f_\nu}{\partial z} \to \frac{f_{\mu+1,\nu} - f_{\mu-1,\nu}}{2\Delta z}, \quad \frac{\partial^2 f_\nu}{\partial z^2} \to \frac{f_{\mu+1,\nu} - 2f_{\mu\nu} + f_{\mu-1,\nu}}{(\Delta z)^2},$$

in which $\Delta z = H/(M-1)$. The resulting set of evolution equations is stepped forward in time using the leapfrog method with an Euler backstep employed every 20 timesteps to prevent splitting errors. Before the solution fields $\omega_{\mu\nu}$ and $\theta_{\mu\nu}$ can be stepped forward in time, we must calculate $\psi_{\mu\nu}$ by inverting (5c), which becomes

$$\omega_{\mu\nu} = \Delta^{(\nu)}_{\mu\kappa} \psi_{\kappa\nu},$$

with summation over κ implied. For each ν, we compute the inverse of the matrix $\Delta^{(\nu)}_{\mu\kappa}$ and multiply it onto the appropriate column of $\omega_{\mu\nu}$. As the matrices $\Delta^{(\nu)}_{\mu\kappa}$ are independent of time, their inverses are calculated only once and then stored on disk for use in the remainder of the simulation.

For the parameter values employed in the present study, we have generally found it sufficient to use a timestep $\Delta t = 0.0375$ (in non-dimensional units), $M = 251$ vertical grid points, and $N = 96$ horizontal modes, although it has been necessary for some simulations to increase N to 120 modes.

To prevent the solutions from becoming excessively contaminated by small-scale noise, we apply a low-pass filter to the dependent fields every 20 timesteps. In the x-direction, the filtering process simply involves multiplying the Fourier coefficients in (4) by a spectral transfer function

$$F_\nu = \begin{cases} 1 & \text{if} \quad \nu < N_f, \\ \frac{1}{2}(1+c) + \frac{1}{2}(1-c)\cos\left(\pi\frac{\nu - N_f}{N - N_f}\right) & \text{if} \quad N_f < \nu < N, \end{cases} \tag{6}$$

in which $c = 0.2$ and $N_f = 0.67N$. In the z-direction, we apply a real-space smoothing operator

$$f_{\mu\nu} \to \sum_{k=0}^{K} \frac{1}{2}A_k(f_{\mu+k,\nu} + f_{\mu-k,\nu}), \tag{7}$$

with $K = 7$ and $A_0 = 0.82$, $A_1 = 0.324354$, $A_2 = -0.233872$, $A_3 = 0.127566$, $A_4 = -0.043663$, $A_5 = 0$, $A_6 = 0.009539$ and $A_7 = -0.003924$, which has spectral properties equivalent to (6). The result is that while medium and large-scale features are damped only by the Laplacian diffusion terms in (2), small-scale features experience an additional damping influence which is equivalent, at the smallest resolvable scales, to a decrease in the Reynolds number from 400 to approximately 140. It should be noted that while this low-pass filtering procedure directly affects only those features which are characterized by lengthscales less than 1.5 times the smallest resolvable scale, nonlinear interactions could in principle distribute the effects of the filtering process to larger-scale features. However, comparison of the results to be displayed here with results from test simulations performed at higher resolution and without filtering indicates that filtering effects are, in fact, confined to small scales.
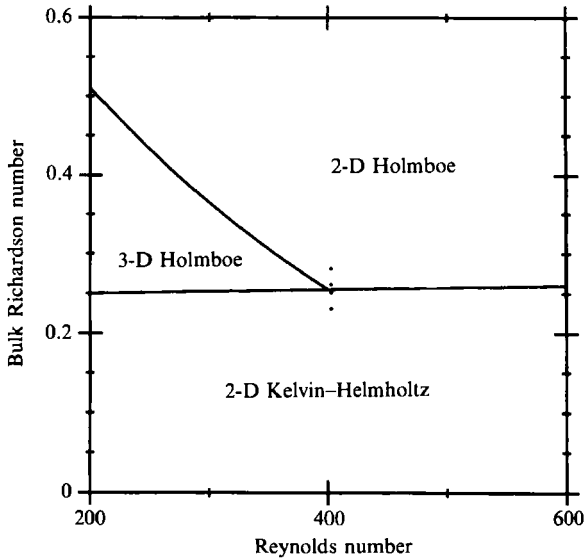
FIGURE 1. Regimes of instability for the stratified shear flow (1), with $R = 3$ and $Pr = 9$. Dots indicate points for which further analyses are presented.

An important consideration in the design of these simulations is the fact that the action of diffusion on the mean flow tends to broaden the shear layer and the stratified layer so as to cause the effective values of α and Ri to increase in time (Smyth *et al.* 1988). In the vicinity of the KH–Holmboe transition, this can have a marked effect on the evolution of the waves which would obscure the phenomena which we wish to investigate. In order that the properties of the finite-amplitude wave may correspond as closely as possible to the stability characteristics of the original stratified shear flow, we arrange for waves to attain finite amplitude early in the simulation by initializing the model with a disturbance that has identical spatial structure to that of the fastest-growing eigenmode of the original parallel flow. The amplitude of this disturbance is chosen to be as large as is consistent with the linearization of the equations employed to perform the stability analysis. The eigenmodes are computed via a Galerkin technique which is described in detail in Smyth & Peltier (1990). We emphasize that the eigenfunction initialization just described has been employed only in the interests of computational efficiency. Auxiliary simulations have been conducted in order to ensure that the important features which have been observed in the evolving flows are not strongly dependent on the initial conditions.

2.2. *Results*

In this subsection we shall present results from four simulations which have been performed using $Re = 400$, $\alpha = 0.3$ and $Ri = 0.28$, 0.26, 0.25 and 0.23. These points in parameter space are indicated by dots on figure 1. The outer points, $Ri = 0.28$ and $Ri = 0.23$, lie relatively far inside the Holmboe and Kelvin–Helmholtz regimes, respectively, while the inner points, $Ri = 0.26$ and $Ri = 0.25$, lie close to the KH–Holmboe transition, which is located at approximately $Ri = 0.255$. These flows lie just outside the region of parameter space in which the primary instability is three-dimensional (cf. §1), and are thus representative of the large class of stratified shear flows which cannot achieve three-dimensionality except via secondary
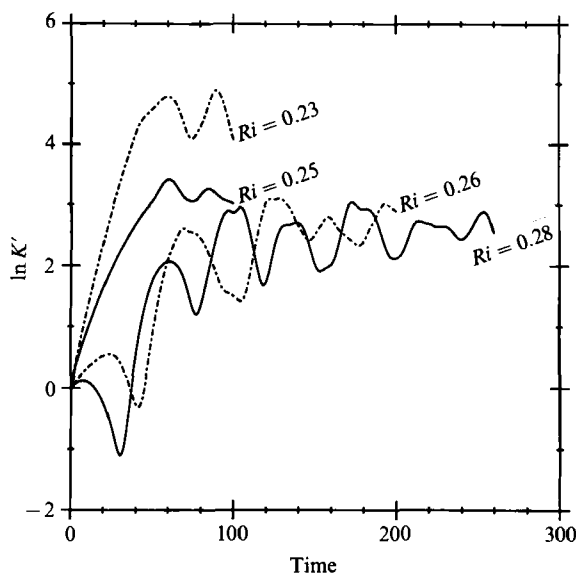
FIGURE 2. Natural logarithm of the wave kinetic energy for simulations employing bulk Richardson numbers $Ri = 0.28$, 0.26, 0.25 and 0.23.

instability. Each simulation was terminated near the state of maximum wave kinetic energy (see (8) below), by which time strong three-dimensional instability was invariably evident.

Figure 2 shows the time history of the wave kinetic energy K', which is defined by

$$K' = \frac{1}{L}\int_0^H \mathrm{d}z \int_0^L \mathrm{d}x\,[(\psi_z - \bar{\psi}_z)^2 + \psi_x^2], \quad \bar{\psi} \equiv \frac{1}{L}\int_0^L \mathrm{d}x\,\psi, \tag{8}$$

for each of these four simulations. It is clear that the Kelvin–Helmholtz waves at $Ri = 0.23$ and $Ri = 0.25$ grow monotonically to maximum amplitude, while the Holmboe waves at $Ri = 0.26$ and $Ri = 0.28$ are oscillatory throughout their evolution. The KH–Holmboe transition is thus located in accordance with the prediction of linear theory.

The spatial forms of the potential temperature and vorticity fields associated with the two-dimensional Holmboe and Kelvin–Helmholtz waves are also useful diagnostics. They are most clearly represented by contour plots corresponding to selected points in the time evolution of the wave. The spacing between the θ contours is the same for all such representations to be described below, as is the spacing between the ω contours. The simulations will be discussed in order of descending bulk Richardson number, i.e. moving from the Holmboe regime into the Kelvin–Helmholtz regime. In the $Ri = 0.28$ and $Ri = 0.23$ cases, we will be mainly interested in noting factors which may influence the stability of the finite-amplitude Holmboe and Kelvin–Helmholtz waves to three-dimensional perturbations. In the cases $Ri = 0.26$ and $Ri = 0.25$, we will focus attention upon certain nonlinear aspects of the structural relationship between Holmboe and Kelvin–Helmholtz waves which have not been previously observed.

Figures 3 (a, b) and 4 contain selected θ and ω plots for the Holmboe wave with $Ri = 0.28$. This sequence of figures encompasses roughly one period of the oscillation which characterizes this class of waves. Clearly visible are the counterpropagating
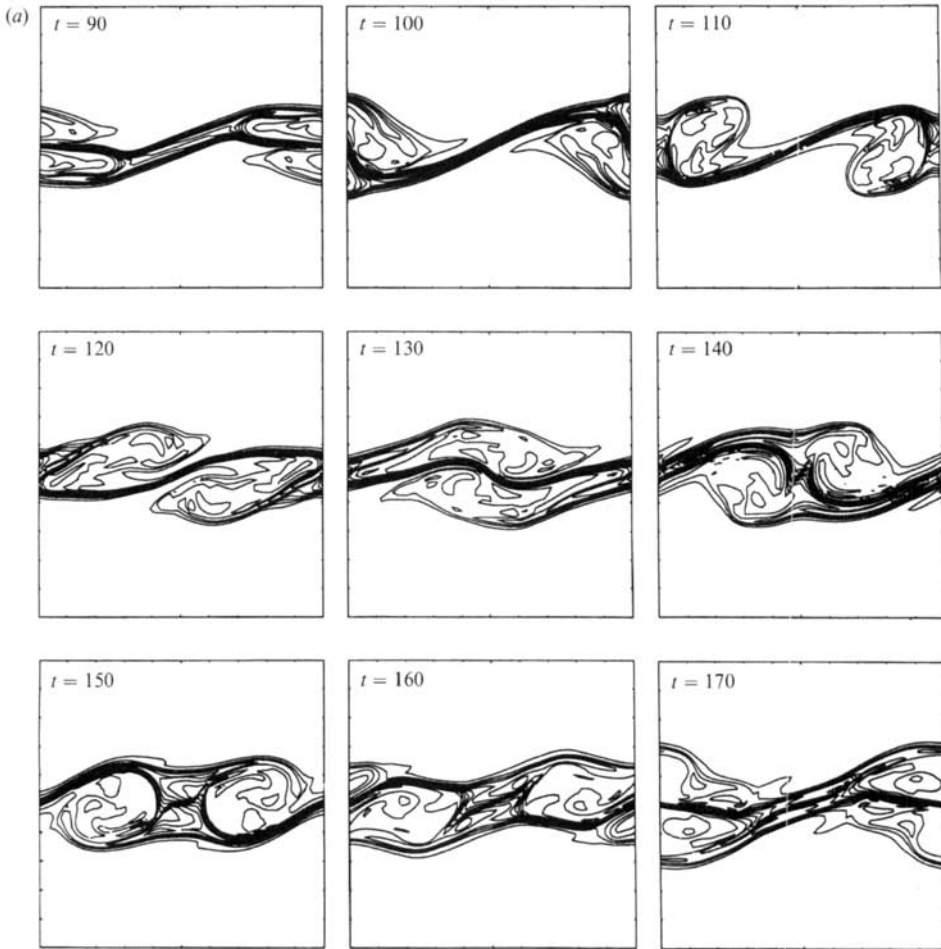
FIGURE 3 (a). For caption see facing page.

component modes which were discussed in detail by Smyth *et al.* (1988) and by Holmboe (1962). In contrast to the more strongly stratified cases investigated by Smyth *et al.* (1988), we observe here an extreme degree of interaction between the upper and lower modes. Plume ejection begins just after the component modes pass each other (e.g. $t = 190$; plume tips are indicated by arrows on figure 3b). The resulting plumes involve the entire stratified layer, inducing large distortions and even overturning in the central potential temperature interface, on which $\theta = 0$ (e.g. $t = 240$; the region of overturned $\theta = 0$ contours is indicated by an arrow). Although local shear acts to suppress convective instability in this two-dimensional flow, and the overturning of the central temperature interface is therefore subsequently reversed, we will see in the next section that the wave is strongly unstable to three-dimensional convective activity at these points in its evolution. In contrast to these transitory overturning events, weaker static instability in the outer regions of the plumes persists throughout most of the wave's oscillatory cycle. As is evident upon inspection of figure 4 (also see Smyth *et al.* 1988), the plumes contain strong gradients of vorticity, which may also be expected to contribute to the secondary instability of the finite-amplitude wave.
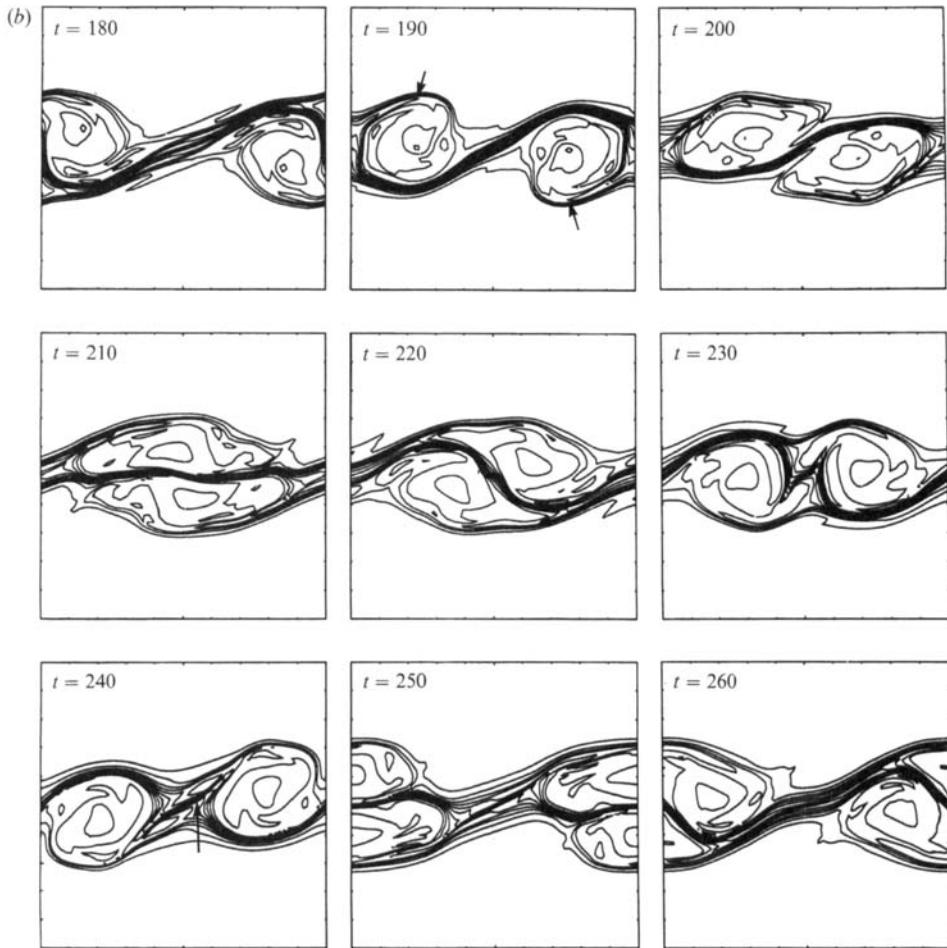
FIGURE 3. (a) Contours of the potential temperature deviation field at selected times for the Holmboe wave at $Ri = 0.28$. (b) Continuation of figure 3(a). Arrows indicate: plume tips at $t = 190$, region of strong convective instability at $t = 240$.

In figures 5 and 6, we present selected potential temperature and vorticity fields for the case $Ri = 0.26$, which is just slightly to the Holmboe side of the KH–Holmboe transition. The evolution which we observe here is distinctly different from that predicted by linear theory. Although the wave grows to finite amplitude in a manner characteristic of Holmboe instability, it subsequently experiences an overturning of the central temperature interface (beginning at $t = 130$, see arrows on figure 5) which is sufficient in degree and duration to overcome the stabilizing effect of the local shear and cause a nonlinear roll-up which leads to the formation of a vortex structure which is very similar to a Kelvin–Helmholtz wave. The alternating regions of positive and negative vorticity which are characteristic of Kelvin–Helmholtz vortices (e.g. Klaassen & Peltier 1985a; Smyth *et al.* 1988) are visible in the vorticity fields which are displayed in figure 6. While remnants of the counterpropagating components modes of the Holmboe wave are still identifiable, it is clear that the 'KH' structure has entrained most of the wave energy. This result suggests that the level of stratification needed to sustain Holmboe waves at finite amplitude may be somewhat in excess of that predicted by linear theory.
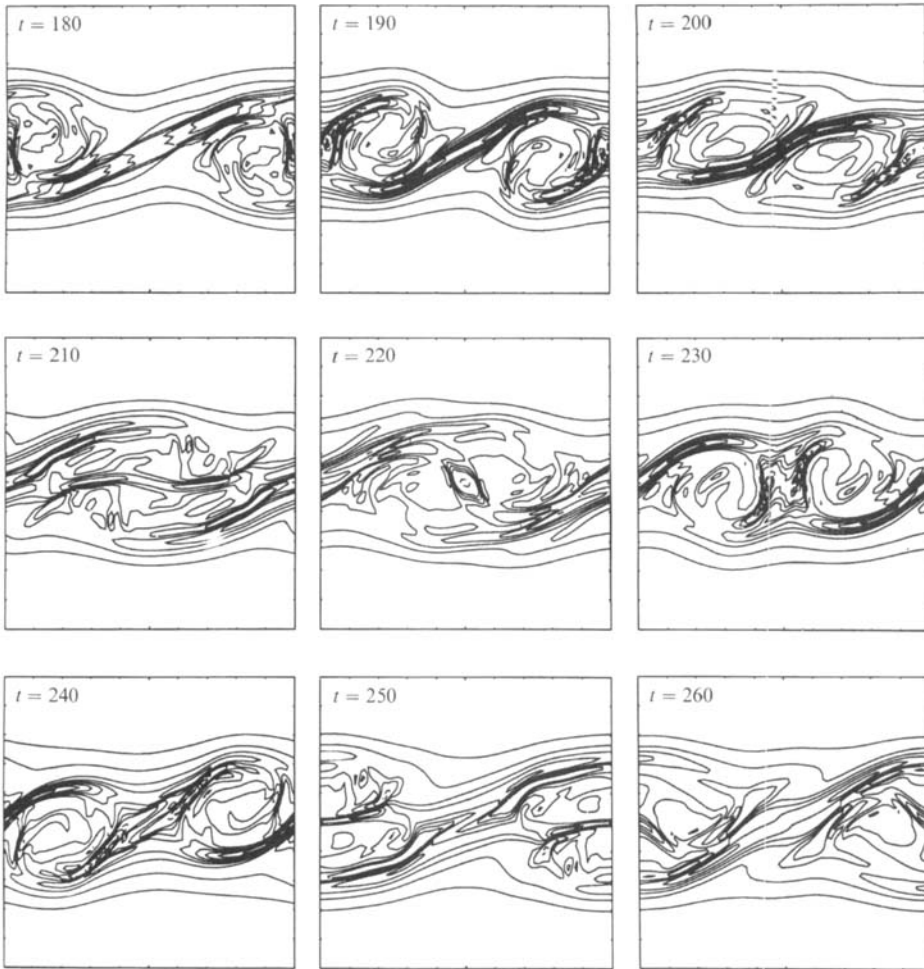
FIGURE 4. Contours of the vorticity field at selected times for the Holmboe wave at $Ri = 0.28$.

Potential temperature fields for the case $Ri = 0.25$ are shown in figure 7. This value of Ri lies slightly to the KH side of the KH–Holmboe transition. Until $t = 60$, this disturbance differs little from a Holmboe wave. Distinct upper and lower component modes are clearly visible at $t = 50$, a feature which is never observed in Kelvin–Helmholtz waves at weaker stratification, but the stratification is not quite strong enough to allow the modes to propagate independently, and they subsequently roll up to form a Kelvin–Helmholtz vortex. The evolution of the wave shown in figure 7 could also be interpreted in terms of resonant wave interactions (e.g. Collins & Maslowe 1988). In this context, one observes that the nonlinear interaction between the dominant mode ($\alpha = 0.3$) and its first harmonic ($\alpha = 0.6$) causes the latter to be strongly excited during the initial evolution of the flow. The resulting waveform is strikingly similar to that which evolves when a pair of KH vortices amalgamates due to subharmonic instability (e.g. figure 5 of Collins & Maslowe 1988). The results of the simulations at $Ri = 0.26$ and $Ri = 0.25$ indicate that the relationship between KH and Holmboe waves in the vicinity of the KH–Holmboe transition is complicated considerably by nonlinear effects.

In figure 8, we present selected θ fields for the final case in this sequence, in which

FIGURE 5. Contours of the potential temperature deviation field at selected times for the 'marginal' Holmboe wave at $Ri = 0.26$. Arrows indicate regions of strong convective instability.

$Ri = 0.23$. This value of Ri locates the flow well inside the KH regime. The evolution of the wave is similar in a broad sense to that observed in the case $Ri = 0.25$ (cf. figure 7), but there is no trace of the distinct upper and lower component modes which were so clearly visible in that case. It will be noted that the form of the wave at finite amplitude is considerably more complex than the simple 'cat's eye' structure that is associated with Kelvin–Helmholtz waves at smaller Prandtl number. The interweaving 'fingers' of hot and cold fluid identified by Klaassen & Peltier (1985a) do not, in the present case, roll up into a smooth spiral but rather behave in a manner reminiscent of thermal plumes, as the intense temperature gradients which this high-Prandtl-number system can support generate regions of strong convective instability. As will be seen in the next section, these regions also support intense three-dimensional secondary instability.
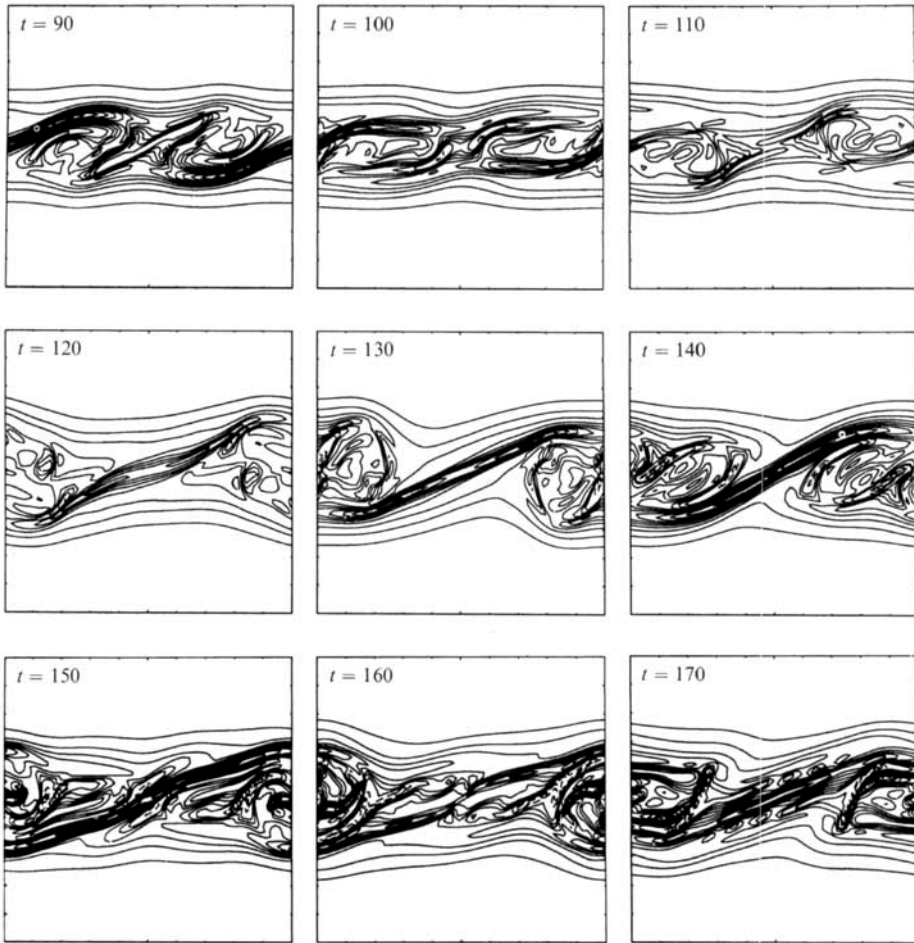
FIGURE 6. Contours of the vorticity field at selected times for the 'marginal' Holmboe wave at $Ri = 0.26$.

3. Three-dimensional stability analysis

3.1. *Methodology*

In this subsection, we shall describe the methods developed to test the stability of the previously discussed two-dimensional nonlinear wave states to three-dimensional perturbations. The method we shall employ to conduct these analyses is based on that described by Klaassen & Peltier (1985*b*), to which the reader may refer for additional detail. This methodology is itself based upon the earlier work of Clever & Busse (1974) on the stability of two-dimensional convection rolls against arbitrary three-dimensional fluctuations.

As in §2, we begin with the Boussinesq equations for a thermally stratified flow. As the flows being considered are no longer two-dimensional, however, we must abandon the vorticity-streamfunction formulation (2) and describe the basic state in terms of the streamwise and vertical velocity fields $\tilde{U}$ and $\tilde{W}$, together with the potential temperature deviation $\tilde{\theta}$. Note that tildes are used to distinguish the two-dimensional wave fields computed in §2 from the three-dimensional perturbation fields which we shall now introduce.
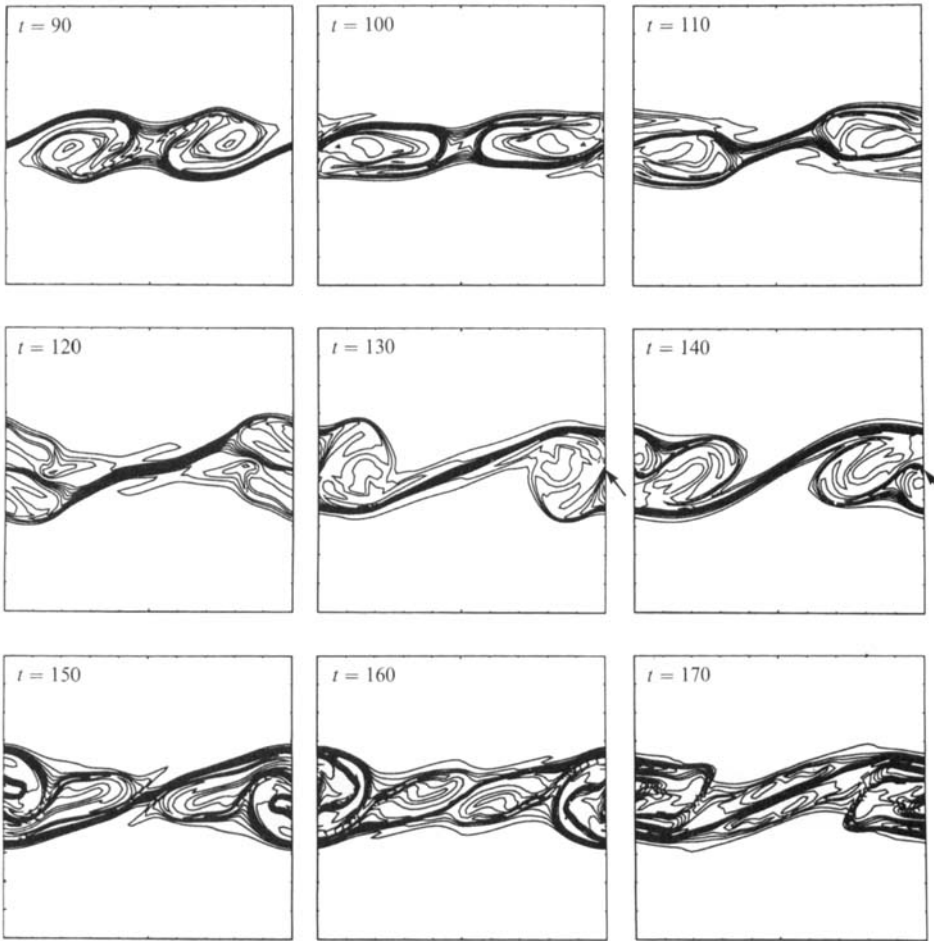
FIGURE 7. Contours of the potential temperature deviation field at selected times for the 'marginal' Kelvin–Helmholtz wave at $Ri = 0.25$.

In the present analyses, we shall consider only those disturbances having the same streamwise periodicity as the basic state wave. (It might be supposed that the evolution of the Holmboe wave will be strongly influenced by other classes of instability, such as those involving subharmonics of the basic state wave, but consideration of these modes is beyond the scope of the present work. See §4 for further discussion of this issue.) Furthermore, we assume, subject to justification *a posteriori*, that the perturbations evolve on a faster timescale than does the two-dimensional nonlinear wave, so that the time-dependence in the latter may be neglected. These assumptions imply that the velocity, potential temperature and pressure fields in the three-dimensional flow have the Floquet form

$$f(x, y, z, t) = \tilde{f}(x, z) + \epsilon \hat{f}(x, z) \, e^{i(bx+dy)} \, e^{\sigma t}, \qquad (9)$$

in which $\hat{f}(x, z)$ is periodic in x with period $2\pi/\alpha$, σ, b and d are the complex growth rate and real streamwise and spanwise wavenumbers of the disturbance, respectively, and ϵ is an ordering parameter. Note that the total fields are periodic in x only if b is commensurate with α. The longitudinally symmetric disturbances which we
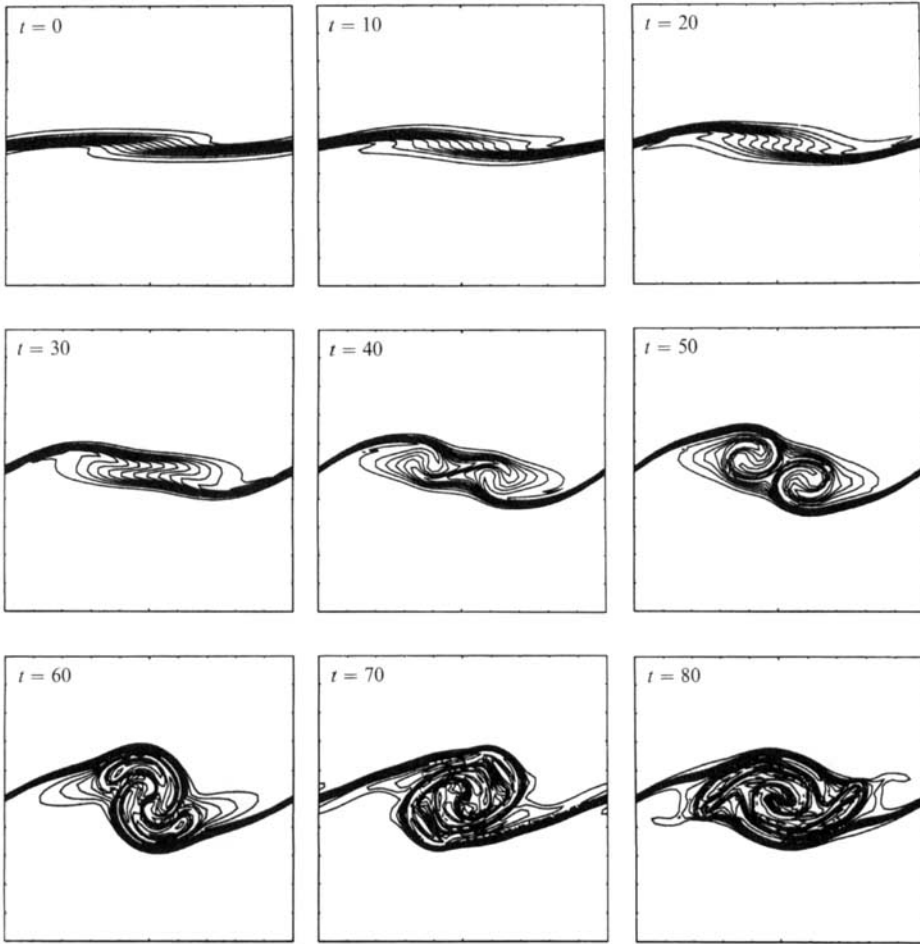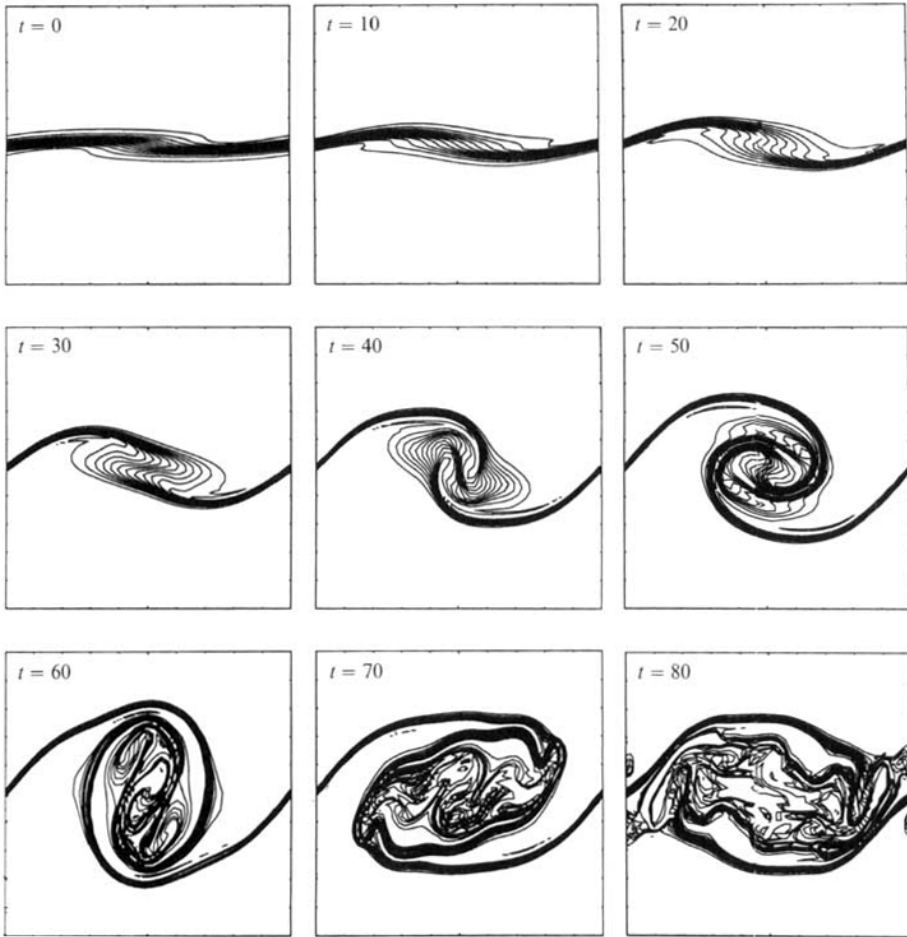
FIGURE 8. Contours of the potential temperature deviation field at selected times for the Kelvin–Helmholtz wave at $Ri = 0.23$.

investigate here have $b = 0$, but we will present the equations in the more general form for $b \neq 0$.

Substituting (9) into the Boussinesq equations we obtain, at order ϵ,

$$\sigma \hat{u} = -\tilde{U}(\partial_x + ib)\,\hat{u} - \tilde{W}\hat{u}_z - (\partial_x + ib)\,\tilde{U}\hat{u} - \tilde{U}_z\hat{w} - (\partial_x + ib)\,\hat{p} + Re^{-1}\nabla^2\hat{u}; \qquad (10)$$

$$\sigma \hat{v} = -\tilde{U}(\partial_x + ib)\,\hat{v} - \tilde{W}\hat{v}_z - id\hat{p} + Re^{-1}\nabla^2\hat{v}; \qquad (11)$$

$$\sigma \hat{w} = -\tilde{U}(\partial_x + ib)\,\hat{w} - \tilde{W}\hat{w}_z - (\partial_x + ib)\,\tilde{W}\hat{u} - \tilde{W}_z\hat{w} - \hat{p}_z + Ri\hat{\theta} + Re^{-1}\nabla^2\hat{w}; \qquad (12)$$

$$\sigma \hat{\theta} = -\tilde{U}(\partial_x + ib)\,\hat{\theta} - \tilde{W}\hat{\theta}_z - (\partial_x + ib)\,\tilde{\theta}\hat{u} - \tilde{\theta}_z\hat{w} + (RePr)^{-1}\nabla^2\hat{\theta}; \qquad (13)$$

$$0 = (\partial_x + ib)\,\hat{u} + id\hat{v} + \hat{w}_z, \qquad (14)$$

in which $\hat{u}$, $\hat{v}$, $\hat{w}$, $\hat{\theta}$ and $\hat{p}$ are the (x, z)-dependent parts of the streamwise, spanwise and vertical velocity, potential temperature and pressure perturbations, respectively. Subscripts indicate partial derivatives, and the Laplacian operator ∇^2 becomes $(\partial_x + ib)^2 + \partial_{zz} - d^2$. A diagnostic equation for the pressure is obtained by combining (10), (12) and (14), viz.

$$\nabla^2\hat{p} = Ri(\partial_x + ib)\,\hat{\theta} - 2((\partial_x + ib)\,\tilde{U}(\partial_x + ib)\,\hat{u} + \tilde{W}_z\hat{w}_z + (\partial_x + ib)\,\tilde{W}\hat{u}_z + \tilde{U}_z(\partial_x + ib)\,\hat{w}).$$

$$(15)$$

We replace (14) with (15), and find as a result that (11) decouples from the remainder of the system. We are thus left with four equations, (10), (12), (13) and (15) for the dependent fields $\hat{u}$, $\hat{w}$, $\hat{\theta}$ and $\hat{p}$. In addition we have (11) and (14), which may be used to compute the spanwise velocity field in two independent ways and thus verify the accuracy of the computations.

In order to convert these equations into an eigensystem, we must discretize the (x, z)-dependence of the solution fields. This is accomplished via the Galerkin method, using the expansions

$$\hat{u} = \sum_{\lambda=-L}^{L} \sum_{\nu=0}^{N} u_{\lambda\nu} F_{\lambda\nu}, \quad \hat{w} = \sum_{\lambda=-L}^{L} \sum_{\nu=0}^{N} w_{\lambda\nu} G_{\lambda\nu},$$
$$\hat{\theta} = \sum_{\lambda=-L}^{L} \sum_{\nu=0}^{N} \theta_{\lambda\nu} G_{\lambda\nu}, \quad \hat{p} = \sum_{\lambda=-L}^{L} \sum_{\nu=0}^{N} p_{\lambda\nu} F_{\lambda\nu}, \tag{16}$$

in which

$$F_{\lambda\nu} = \mathrm{e}^{\mathrm{i}\lambda\alpha x} \cos\frac{\nu\pi z}{H}, \quad G_{\lambda\nu} = \mathrm{e}^{\mathrm{i}\lambda\alpha x} \sin\frac{\nu\pi z}{H}. \tag{17}$$

Following Klaassen & Peltier (1985*b*), we employ the truncation scheme

$$L(\nu) = \left[\frac{N-\nu}{2} - \frac{b}{\alpha}\right],$$

in which N is an odd integer and square brackets indicate the largest integer not exceeding the value of the enclosed quantity. Owing to the limited main memory on the machines available to us, we must restrict the truncation parameter N to values not exceeding 29. Resolution tests indicate that this truncation level is adequate for our present purposes. We now substitute (16) into the perturbation equations (10), (12), (13) and (15) and diagonalize the left-hand side of the system by taking the appropriate inner products. Equation (15) is then solved for $p_{\lambda\nu}$ and the result substituted into (10) and (12), leaving us with the following set of linear algebraic equations for the coefficients $u_{\lambda\nu}$, $w_{\lambda\nu}$ and $\theta_{\lambda\nu}$:

$$\sigma u_{\kappa\mu} = \langle UU \rangle_{\kappa\mu}^{\lambda\nu} u_{\lambda\nu} + \langle UW \rangle_{\kappa\mu}^{\lambda\nu} w_{\lambda\nu} + \langle UT \rangle_{\kappa\mu}^{\lambda\nu} \theta_{\lambda\nu}, \tag{18a}$$

$$\sigma w_{\kappa\mu} = \langle WU \rangle_{\kappa\mu}^{\lambda\nu} u_{\lambda\nu} + \langle WW \rangle_{\kappa\mu}^{\lambda\nu} w_{\lambda\nu} + \langle WT \rangle_{\kappa\mu}^{\lambda\nu} \theta_{\lambda\nu}, \tag{18b}$$

$$\sigma \theta_{\kappa\mu} = \langle TU \rangle_{\kappa\mu}^{\lambda\nu} u_{\lambda\nu} + \langle TW \rangle_{\kappa\mu}^{\lambda\nu} w_{\lambda\nu} + \langle TT \rangle_{\kappa\mu}^{\lambda\nu} \theta_{\lambda\nu}. \tag{18c}$$

Explicit expressions for the four-dimensional coefficient arrays $\langle UU \rangle$, $\langle UW \rangle$, etc. may be found in the Appendix. Equation (18) may be written in the form $\sigma V_i = A_{ij} V_j$, in which A is a constant matrix and V is the concatenation of $\{u_{\lambda\nu}, w_{\lambda\nu}, \theta_{\lambda\nu}\}$.

Eigenvalues of A are computed using routines from the EISPACK library (Smith *et al.* 1977). Selected eigenvectors are computed using the subroutine CHEVEC (Klaassen & Peltier 1985*b*), which requires considerably less core memory than does the corresponding EISPACK routine.

The dynamical processes which govern the evolution of a given disturbance may be diagnosed by means of the perturbation kinetic energy equation, which may be written in the form

$$\sigma_{\mathrm{r}} = \mathscr{S}h + \mathscr{S}t + Ri\mathscr{H} + \mathscr{D}/Re, \tag{19}$$

in which

$$K' = \langle (\hat{u}^*\hat{u} + \hat{v}^*\hat{v} + \hat{w}^*\hat{w}) \rangle; \tag{20}$$

$$\mathscr{S}h = -\langle (\tilde{W}_x + \tilde{U}_z)(\hat{u}^*\hat{w})_{\mathrm{r}} \rangle/K'$$

$$\mathscr{S}t = -\langle \tfrac{1}{2}(\tilde{U}_x - \tilde{W}_z)(\hat{u}^*\hat{u} - \hat{w}^*\hat{w}) \rangle/K'$$

$$\mathscr{H} = \langle (\hat{w}^*\hat{\theta})_{\mathrm{r}} \rangle/K'$$

$$\mathscr{D} = \langle (\hat{u}^*\nabla^2\hat{u} + \hat{v}^*\nabla^2\hat{v} + \hat{w}^*\nabla^2\hat{w})_{\mathrm{r}} \rangle/K' \tag{21}$$
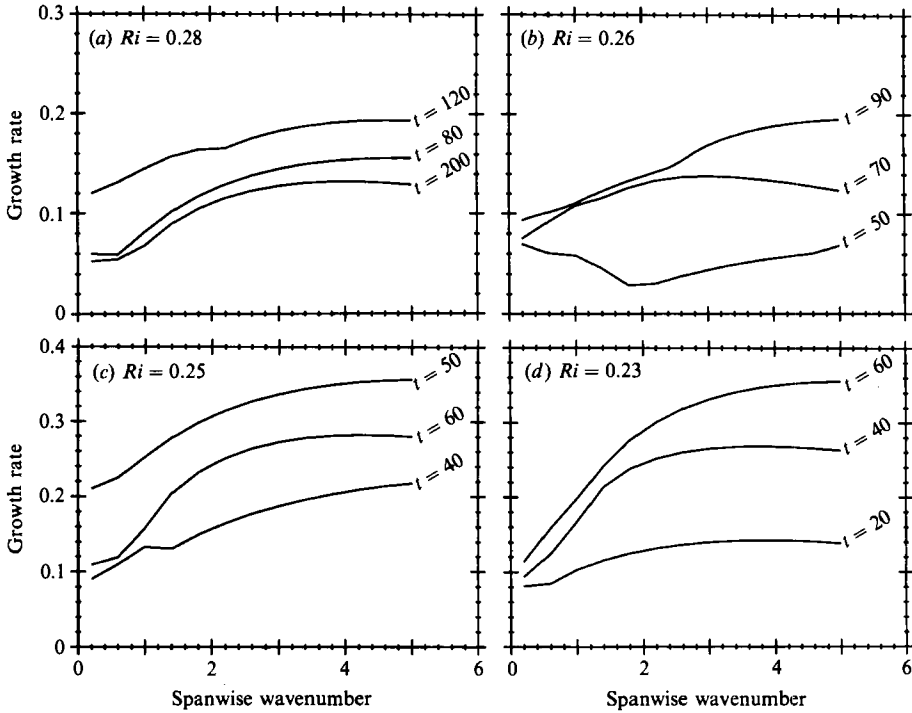
FIGURE 9. Growth rate versus spanwise wavenumber for the fastest-growing three-dimensional disturbance at selected times during the $Ri = 0.28$, 0.26, 0.25 and 0.23 simulations.

(Klaassen & Peltier 1991; following Laprise & Peltier 1989), in which stars represent complex conjugates and angle brackets represent the integral

$$\langle \ \rangle \equiv \frac{2\pi}{\alpha} \int_0^{2\pi/\alpha} \frac{2\pi}{d} \int_0^{2\pi/d} \int_0^H \mathrm{d}x\,\mathrm{d}y\,\mathrm{d}z.$$

The terms on the right-hand side of (19) represent contributions to the growth of the perturbation kinetic energy K' due to the shearing and straining deformations of the basic state velocity fields, convection associated with unstable potential temperature gradients, and dissipation due to viscosity, respectively.

3.2. Results

In figure 9, we show the growth rates of the dominant longitudinal normal modes as functions of the spanwise wavenumber d at selected times during each of the four simulations described in §2. In previous studies of a similar nature (e.g. Klaassen & Peltier 1985b, 1985c, 1991), $\sigma_r(d)$ has been shown to exhibit a strong local maximum, typically in the vicinity of $d = 3$. This indicates a secondary instability with a well-defined spanwise wavelength which should lead the flow into a complex, but nonetheless laminar, three-dimensional state. In contrast, we observe here a general tendency for σ_r to increase monotonically to large spanwise wavenumbers. (Similar results have been obtained by Orszag & Patera (1980) in the study of planar channel flows, and by Pierrehumbert & Widnall (1982) and Klaassen & Peltier (1991) in the analysis of longitudinal instabilities of the Stuart vortex.) Although dissipation must ultimately reduce the growth rate at sufficiently small scales of motion, and extended calculations (not shown here) reveal that σ_r generally reaches a maximum around $d = 5$, there is no evidence of a strongly preferred spanwise wavenumber. We thus

conclude that longitudinal instability of these flows is capable of injecting energy into very small scales of motion, and over a broad region of the wavenumber spectrum. This result suggests that secondary instability should lead these flows directly into the turbulent state.

In the remainder of this section, we will examine these unstable modes in detail. We will identify the spatial locations at which the amplitudes of the instabilities are greatest, and we will discover the manner in which the instabilities vary on the 'slow' timescale associated with the evolution of the basic state wave. We will also seek to identify, via the energy equation (19), the physical processes which are responsible for these secondary instabilities.

In figures 10, 12, 14 and 16, we display in compact form the data which are required in order to obtain the types of information mentioned in the preceding paragraph. The field represented by the solid contours is $\dot{K}' \equiv \sigma_r K'(x, z)$, $K'(x, z)$ being the integrand appearing on the right-hand side of (20), averaged over one wavelength in the spanwise direction. The eigenfunctions are normalized so that the global maximum of $K'(x, z)$ is unity. The density of the contours thus indicates visually the rate at which the perturbation kinetic energy grows at each location (x, z). The unstable eigenmodes which the flow possesses at each point in time are numbered sequentially (mode 1, mode 2, etc.) in order of descending growth rate, and we display $\dot{K}'$ for mode 1 and also for one of the weaker modes. The latter is usually mode 2, but in some cases the third-strongest mode is of greater interest and we display that mode instead. The dotted curves appearing on the upper figures are loosely-spaced contours of the basic potential temperature field $\tilde{\theta}$, which we include so that the location of the mode with respect to the two-dimensional wave may be seen without referring back to the more detailed representations of the previous section. Finally, each field contains numerical values of σ, $\mathscr{S}_k$, $\mathscr{S}_t$, $\mathscr{H}$ and $\mathscr{D}$. Presentations of these quantities as functions of time are found in separate figures. The choice of a spanwise wavenumber for these calculations is largely arbitrary in view of the results shown in figure 9, and the results tend not to vary significantly with d; the results which we have chosen to display here are for $d = 4$.

In figure 10, we show $\dot{K}'$ for the Holmboe wave at $Ri = 0.28$ during the time interval from $t = 110$ to $t = 260$. What we see in most of these plots is instability located in the plumes of the Holmboe wave, driven primarily by a combination of shear and convective activity, the latter associated with overturned potential temperature contours. An example of this is seen at $t = 110$. The most intense instabilities are found at times such as $t = 120$, when the plume-ejection mechanism has caused temporary overturning of the central temperature interface $\tilde{\theta} = 0$. We will examine the stability characteristics of the wave at this point in its evolution in detail. Mode 1 and mode 2 (not shown) are primarily convective and are located in the 'roots' of the plumes, where static instability is most extreme. Somewhat surprisingly, we find that unstable modes rarely reside in the relatively undistorted regions of the stratified layer, such as the region located at the centre of the $t = 120$ plot, even though the shearing deformation is generally strongest there. The shear-driven mode (mode 3) appearing at $t = 120$ is an exception to this. Mode 4 (not shown) resides in the body of the plume and is similar in appearance to the dominant mode at $t = 110$.

The dominant mode at $t = 130$ is again located in the roots of the plumes where the $\tilde{\theta} = 0$ contour is overturned. Mode 2 is a ring-shaped structure composed of unstable modes located in the upper and lower plumes, which are vertically aligned at this point. This ring-shaped disturbance is observed whenever the component
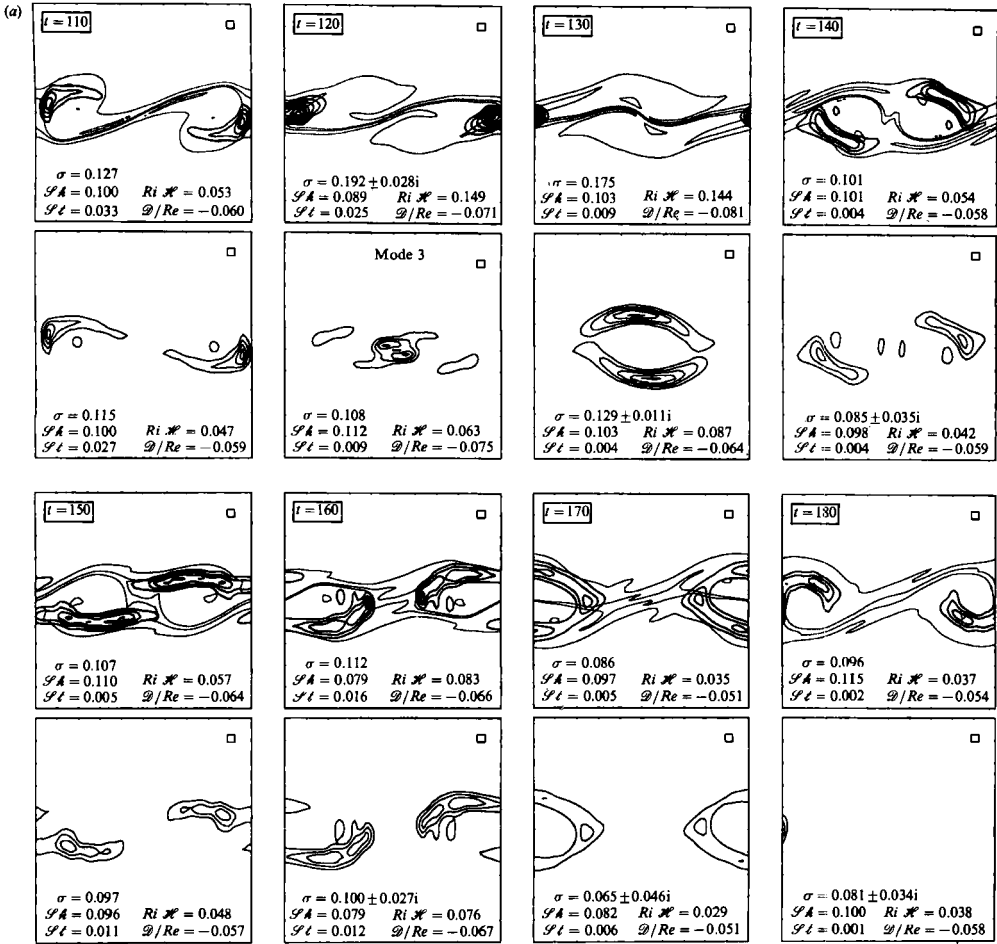
FIGURE 10 (a). For caption see facing page.

modes of the Holmboe wave pass by one another. The weaker eigenmodes are similar in appearance to mode 2. In the remainder of figure 10(a) and in figure 10(b), we continue to observe unstable modes which are associated with the plumes of the Holmboe wave. The ring-shaped structure which we found at $t = 130$ is seen again at $t = 170$, $t = 210$ and $t = 250$, although the convective modes which dominated at $t = 130$ do not appear at these subsequent times because the plume-ejection mechanism has not generated significant overturning in the strongly stratified region near $\tilde{\theta} = 0$. Maximum growth rates occur just prior to these points (i.e. at $t = 120$, 160, 200 and 240), when the spatial extent of the plumes is greatest.

In figure 11(a), we show the growth rate $\sigma_{3D} = \sigma_r$ of the dominant three-dimensional instability as a function of time (solid curve), along with the growth/decay rate of the kinetic energy associated with the two-dimensional wave, viz.:

$$\sigma_{2D} = \frac{1}{2}\frac{1}{K}\frac{dK}{dt}. \tag{22}$$

Over the period $t = 110$–260, the r.m.s. time average of σ_{2D} is 0.02, while the r.m.s. average of σ_{3D} over the same period is 0.10. By this measure, the unstable modes grow on a timescale which is separated by a factor of five from the 'slow' timescale

(b)

$t = 190$
$\sigma = 0.102 \pm 0.006i$
$\mathscr{S}\hbar = 0.090 \quad Ri\,\mathscr{H} = 0.048$
$\mathscr{S}t = 0.031 \quad \mathscr{D}/Re = -0.067$

$t = 200$
$\sigma = 0.132$
$\mathscr{S}\hbar = 0.076 \quad Ri\,\mathscr{H} = 0.099$
$\mathscr{S}t = 0.025 \quad \mathscr{D}/Re = -0.068$

$t = 210$
$\sigma = 0.077$
$\mathscr{S}\hbar = 0.082 \quad Ri\,\mathscr{H} = 0.063$
$\mathscr{S}t = 0.006 \quad \mathscr{D}/Re = -0.074$

$t = 220$
$\sigma = 0.077$
$\mathscr{S}\hbar = 0.109 \quad Ri\,\mathscr{H} = 0.029$
$\mathscr{S}t = 0.011 \quad \mathscr{D}/Re = -0.050$

$\sigma = 0.100$
$\mathscr{S}\hbar = 0.086 \quad Ri\,\mathscr{H} = 0.046$
$\mathscr{S}t = 0.032 \quad \mathscr{D}/Re = -0.064$

$\sigma = 0.114 \pm 0.021i$
$\mathscr{S}\hbar = 0.080 \quad Ri\,\mathscr{H} = 0.084$
$\mathscr{S}t = 0.016 \quad \mathscr{D}/Re = -0.067$

$\sigma = 0.068 \pm 0.044i$
$\mathscr{S}\hbar = 0.081 \quad Ri\,\mathscr{H} = 0.050$
$\mathscr{S}t = 0.007 \quad \mathscr{D}/Re = -0.070$

$\sigma = 0.06 \pm 0.036i$
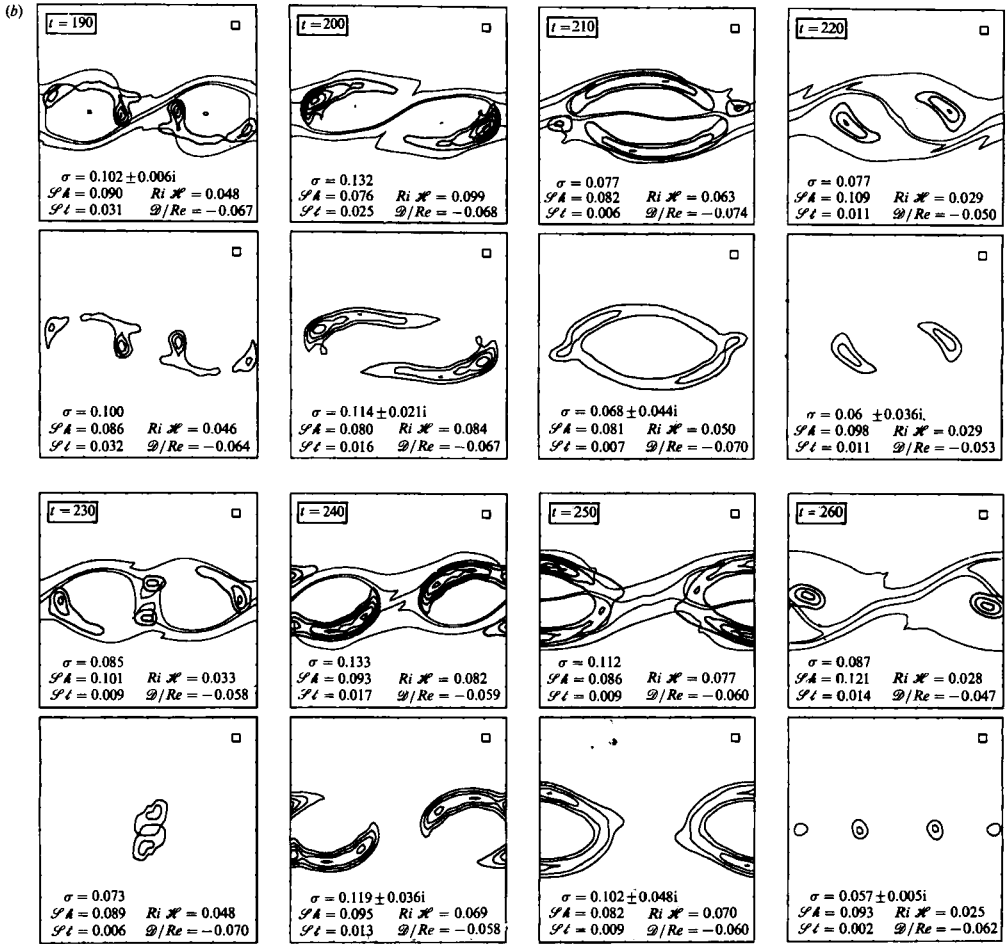$\mathscr{S}\hbar = 0.098 \quad Ri\,\mathscr{H} = 0.029$
$\mathscr{S}t = 0.011 \quad \mathscr{D}/Re = -0.053$

$t = 230$
$\sigma = 0.085$
$\mathscr{S}\hbar = 0.101 \quad Ri\,\mathscr{H} = 0.033$
$\mathscr{S}t = 0.009 \quad \mathscr{D}/Re = -0.058$

$t = 240$
$\sigma = 0.133$
$\mathscr{S}\hbar = 0.093 \quad Ri\,\mathscr{H} = 0.082$
$\mathscr{S}t = 0.017 \quad \mathscr{D}/Re = -0.059$

$t = 250$
$\sigma = 0.112$
$\mathscr{S}\hbar = 0.086 \quad Ri\,\mathscr{H} = 0.077$
$\mathscr{S}t = 0.009 \quad \mathscr{D}/Re = -0.060$

$t = 260$
$\sigma = 0.087$
$\mathscr{S}\hbar = 0.121 \quad Ri\,\mathscr{H} = 0.028$
$\mathscr{S}t = 0.014 \quad \mathscr{D}/Re = -0.047$

$\sigma = 0.073$
$\mathscr{S}\hbar = 0.089 \quad Ri\,\mathscr{H} = 0.048$
$\mathscr{S}t = 0.006 \quad \mathscr{D}/Re = -0.070$

$\sigma = 0.119 \pm 0.036i$
$\mathscr{S}\hbar = 0.095 \quad Ri\,\mathscr{H} = 0.069$
$\mathscr{S}t = 0.013 \quad \mathscr{D}/Re = -0.058$

$\sigma = 0.102 \pm 0.048i$
$\mathscr{S}\hbar = 0.082 \quad Ri\,\mathscr{H} = 0.070$
$\mathscr{S}t = 0.009 \quad \mathscr{D}/Re = -0.060$

$\sigma = 0.057 \pm 0.005i$
$\mathscr{S}\hbar = 0.093 \quad Ri\,\mathscr{H} = 0.025$
$\mathscr{S}t = 0.002 \quad \mathscr{D}/Re = -0.062$

FIGURE 10. (a) Contours of $\dot{K}'(x,z)$ (solid contours) and $\tilde{\theta}(x,z)$ (dotted contours) for three-dimensional disturbances at selected times during the $Ri = 0.28$ simulation. Numerical values are also given for the growth rate and the contribution terms appearing on the right-hand side of (19) for each mode. (b) Continuation of (a).

upon which the basic state evolves. This degree of timescale separation is at least sufficient to ensure that our normal-mode stability calculations deliver a qualitatively accurate representation of the transition to three-dimensional motion.

In figure 11(b), we have plotted the various contributions to $\sigma_{3\mathrm{D}}$ which appear on the right-hand side of (19). It is evident that the term $\mathscr{S}\hbar$, which represents instability due to the shearing deformation of the two-dimensional velocity field, is dominant over most of the wave's history. The convection term $Ri\,\mathscr{H}$ also plays an important role in governing temporal variations in $\sigma_{3\mathrm{D}}$. Local maxima in $\sigma_{3\mathrm{D}}$ generally coincide with maxima in $Ri\,\mathscr{H}$ and with minima in $\mathscr{S}\hbar$. The $\mathscr{S}t$ term, which is associated with the straining deformation in the background flow, is generally of small magnitude. It does, however, make a significant contribution at or just prior to the times of maximum disturbance growth. The dissipation term $\mathscr{D}/Re$ is uniformly negative, as expected.

The quasi-periodicity which is evident in the time dependence of the dominant partial growth rates $\mathscr{S}\hbar$ and $Ri\,\mathscr{H}$ is clearly connected with the oscillatory cycle
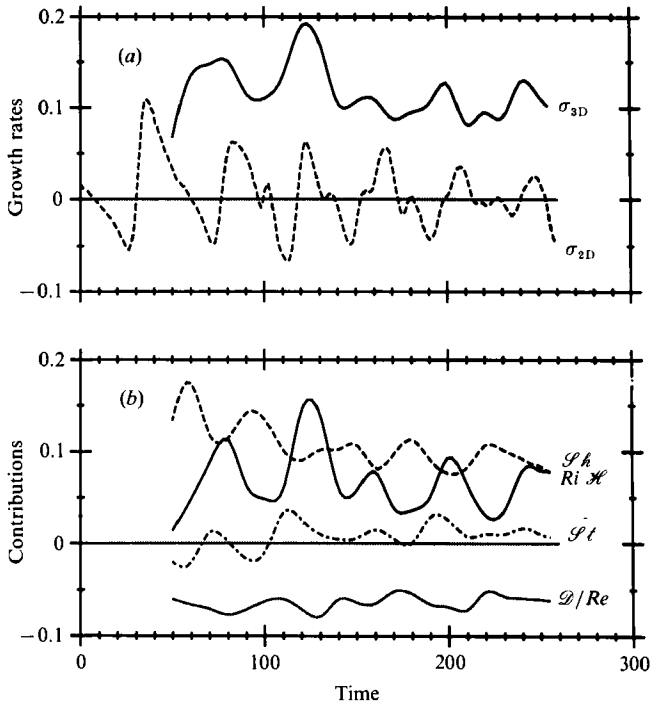
FIGURE 11. (a) Growth rates of ——, the dominant three-dimensional normal mode and –––, the two-dimensional wave for the Holmboe wave at $Ri = 0.28$. (b) Contributions to σ_{3D} appearing on the right-hand side of (19).

which characterizes the Holmboe wave. This oscillation involves a periodic exchange of energy between the potential and wave kinetic energy reservoirs (Smyth *et al.* 1988). During the phase of the oscillation in which the wave kinetic energy is large, we expect to find strong shears which may drive secondary instability. In contrast, the configuration of the wave during times of high potential energy is likely to involve overturning and consequent convective instability. The terms $\mathscr{S}h$ and $Ri\mathscr{H}$ in (19) thus represent alternate mechanisms through which the three-dimensional disturbance may access whichever form of energy is plentiful in the Holmboe wave at a particular time. Comparison of figures 2 and 11 reveals that the results of the present computations are in accord with this scenario.

In figure 12, we show $\dot{K}'(x, z)$ for the 'marginal' Holmboe wave, for which $Ri = 0.26$. The stability results shown cover the time period $t = 60$–130. Prior to $t = 130$, the unstable modes are primarily shear-driven and are usually, though not always, associated with the plumes of the developing Holmboe wave. At $t = 130$, the nonlinear convective roll-up which was noted in §2 generates intense convective instability which persists for the remainder of the simulation.

Growth rates and contributions thereto for the $Ri = 0.26$ wave are shown in figure 13. Figure 13(a) indicates that timescale separation is generally good except in the interval $t = 110$–120, during which the results of the normal-mode stability analysis may not be particularly reliable. Results shown in figure 13(b) illustrate our earlier observation, namely that shear-driven instability dominates until the point at which the Holmboe wave is destroyed by the nonlinear roll-up mechanism and intense convective instability appears.

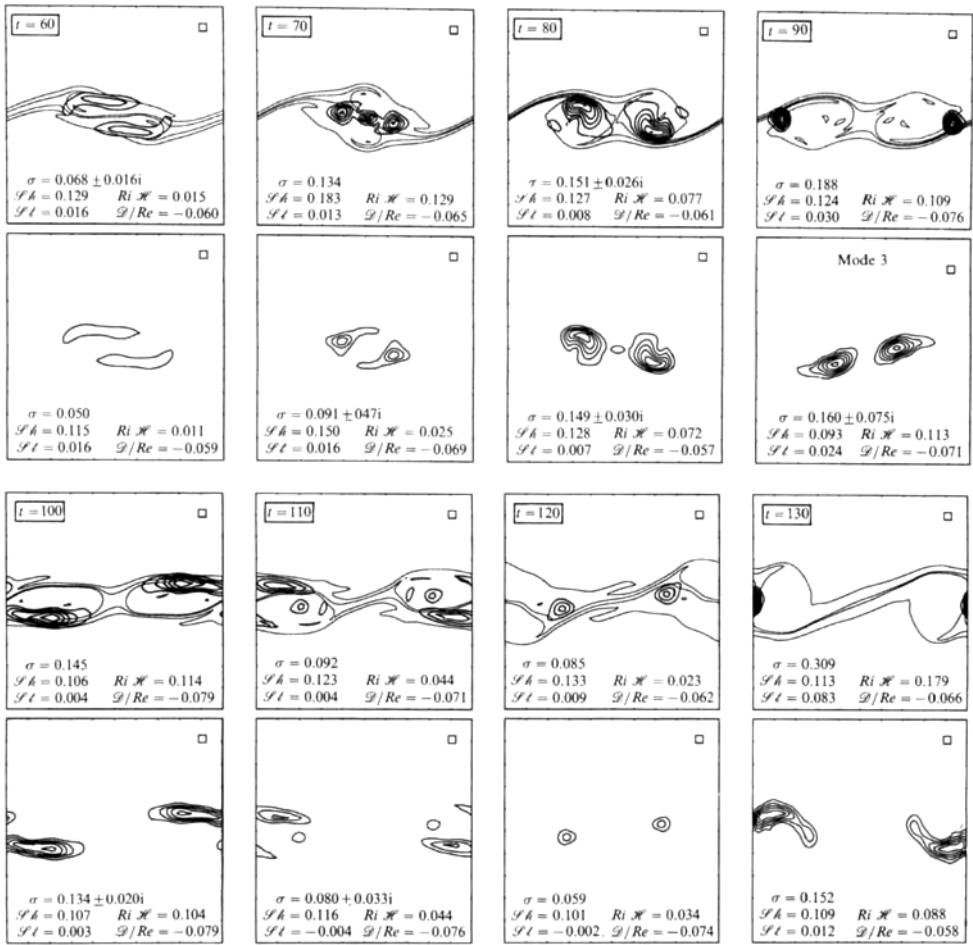Figure 14 contains results from the stability analysis of the 'marginal'

FIGURE 12. Contours of $\dot{K}'(x,z)$ (solid contours) and $\tilde{\theta}(x,z)$ (dotted contours) for three-dimensional disturbances at selected times during the $Ri = 0.26$ simulation.

Kelvin–Helmholtz wave at $Ri = 0.25$. As was seen in §2, the early evolution of this wave features the appearance of distinct, phase-locked component modes which would counterpropagate to produce Holmboe instability if the value of Ri was slightly larger. The $\dot{K}'$ plots for $t = 50$ and $t = 60$ reveal that the stability characteristics of the two-dimensional wave during this time are strongly reminiscent of the results obtained previously for the Holmboe wave (cf. figures 10 and 11). At subsequent times, we find modes driven primarily by convective activity in the statically unstable regions of the evolving Kelvin–Helmholtz vortex (cf. Klaassen & Peltier 1985b, c, 1991).

The growth rates plotted in figure 15(a) confirm that timescale separation is excellent throughout this simulation. As is evident upon inspection of figure 15(b), unstable modes are driven primarily by the shearing deformation of the two-dimensional flow previous to $t = 40$, after which convection becomes the dominant mechanism of instability. Note that the shear term once again increases in importance towards the end of the simulation. Results at that stage must be interpreted with caution, however, owing to evident spatial underresolution.

In figures 16 and 17, we show stability results for the final simulation in the
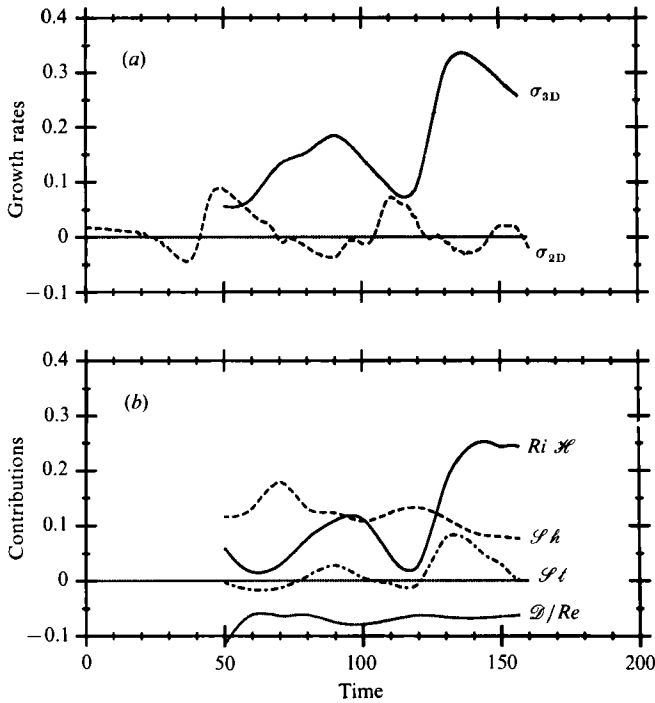
FIGURE 13. (a) Growth rates of ——, the dominant three-dimensional normal mode and ---, the two-dimensional wave for the $Ri = 0.26$ simulation. (b) Contributions to σ_{3D} appearing on the right-hand side of (19).

sequence, namely the Kelvin–Helmholtz wave with $Ri = 0.23$. In the $\dot{K}'$ plots (figure 16), we see once again the successive core-centred and ring-shaped unstable modes which are characteristic of the Kelvin–Helmholtz wave. The shear-driven unstable modes which we observe in the early stages of the wave's evolution are suggestive of the non-scale-selective, shear-driven, longitudinal instability which has been shown by Pierrehumbert (1986) to be a generic feature of non-parallel, inviscid, two-dimensional flows. At $t = 60$, the four strongest modes have nearly identical spatial distributions and have growth rates $\sigma = 0.308$, $0.337 \pm 0.094i$, $0.280 \pm 0.197i$ and $0.161 \pm 0.303i$. The reader will note that the angular frequencies σ_i of these modes fall approximately into a $1:2:3$ ratio which is reminiscent of the spectrum of a time-periodic phenomenon. Since the oscillatory modes occur in complex conjugate pairs, they represent standing waves with nodes distributed in the spanwise direction. At $t = 70$, we observe a similar pattern, with $\sigma = 0.308$, $0.301 \pm 0.057i$, $0.275 \pm 0.110i$ and $0.231 \pm 0.153i$. This 'overtone' pattern has been noted previously by Klaassen & Peltier (e.g. 1985b) in the stability analysis of Kelvin–Helmholtz waves evolving in a flow with $Pr = 1$. The results from the $Ri = 0.23$ case thus show good qualitative agreement with the results of previous stability analyses of Kelvin–Helmholtz waves, with the important exception that the disturbance exhibits no preferred spanwise lengthscale (cf. figure 9 and the accompanying discussion).

    We see upon inspection of figure 17 (a) that we have excellent timescale separation throughout this simulation. The evolution of the partial growth rates (figure 17b) is qualitatively identical to that found for the previous case $Ri = 0.25$ (cf. figure 15b). We see that the shearing deformation provides the primary destabilizing influence near the beginning of the simulation, after which the convective contribution
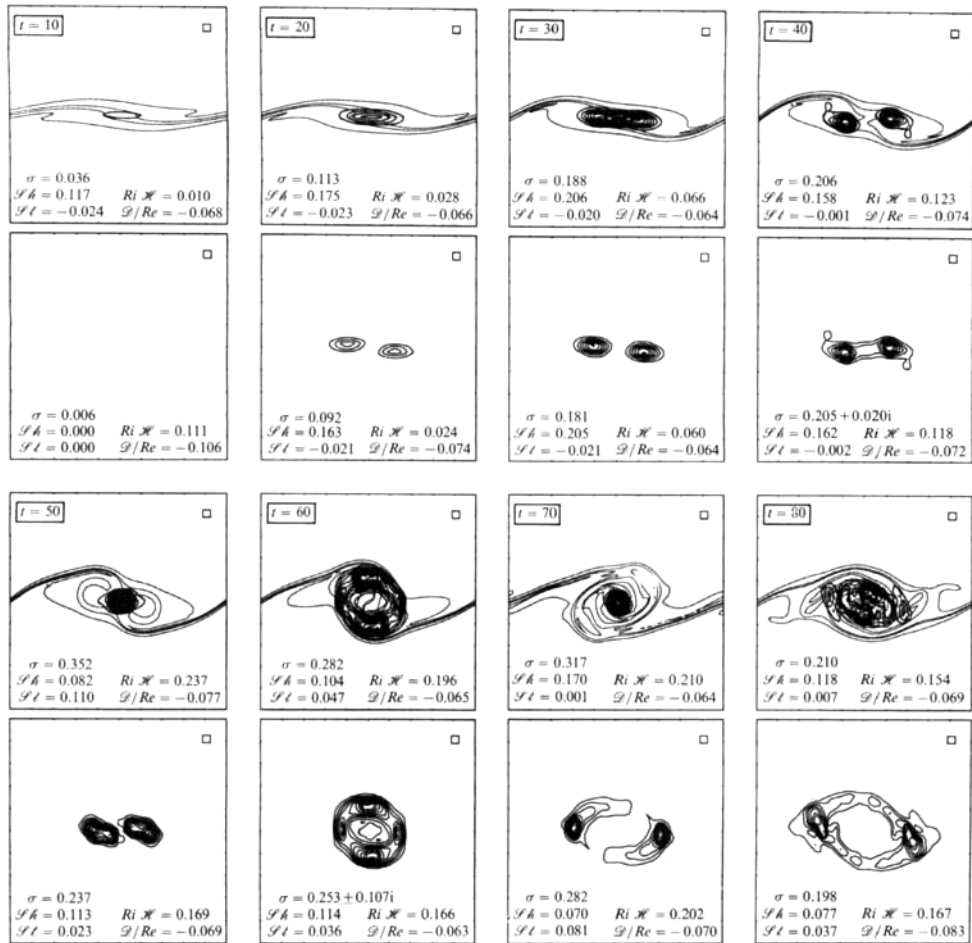
FIGURE 14. Contours of $\dot{K}'(x,z)$ (solid contours) and $\tilde{\theta}(x,z)$ (dotted contours) for three-dimensional disturbances at selected times during the $Ri = 0.25$ simulation.

becomes dominant. Once again, the results pertaining to the later stages of the simulation may be unreliable owing to underresolution, but it appears that the $\mathscr{S}h$ term is again becoming competitive with the convective term. The relative importance of the shear-driven and convective contributions is apparently correlated with the nonlinear oscillation which is evident in figure 2, which is itself associated with the nutation of the vortex core which occurs as the intrusions of dense and light fluid circulate (Klaassen & Peltier 1985a). It appears entirely likely that the $\mathscr{S}h$ and $Ri\mathscr{H}$ terms will, at subsequent times, execute a period out-of-phase oscillation similar to that found for the Holmboe wave (cf. figure 11b).

The time histories of the partial growth rates $\mathscr{S}h$, $\mathscr{S}t$, $Ri\mathscr{H}$ and $\mathscr{D}/Re$ for the four nonlinear wave simulations discussed in this paper exhibit remarkable similarities. In each case we have seen a distinct positive correlation between $\mathscr{S}t$ and $Ri\mathscr{H}$, and a negative correlation between these two terms and $\mathscr{S}h$. These correlations are interesting in themselves, the more so because they are observed in the stability characteristics of two fundamentally dissimilar wave types. It appears that the linear oscillation of the Holmboe wave and the nonlinear oscillation of the Kelvin–Helmholtz wave induce quasi-periodic variations in the two-dimensional
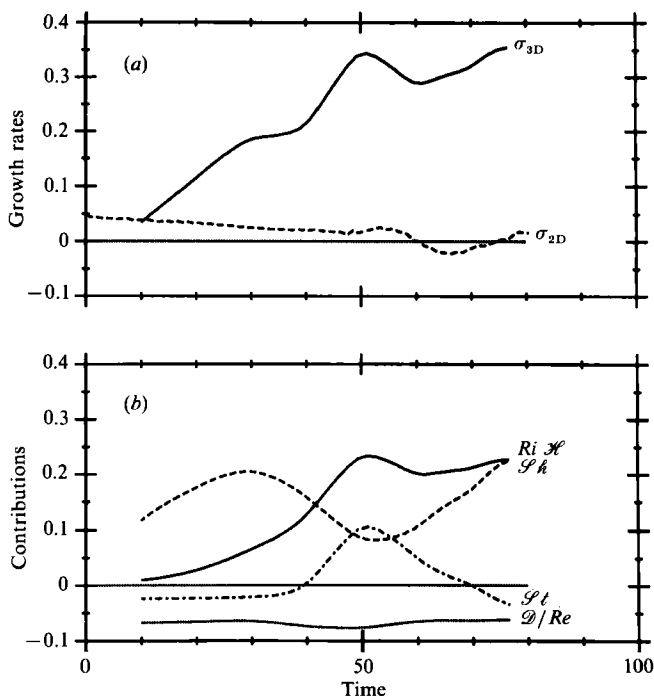
FIGURE 15. (a) Growth rates of ——, the dominant three-dimensional normal mode and ---, the two-dimensional wave for the $Ri = 0.25$ simulation. (b) Contributions to σ_{3D} appearing on the right-hand side of (19).

velocity and potential temperature fields which have very similar effects on the dynamics relevant to three-dimensional secondary instabilities. This periodicity has been explained in the case of Holmboe waves (see the discussion accompanying figure 11b), and it seems likely that a similar mechanism operates in the case of Kelvin–Helmholtz waves (i.e. that the quasi-periodic exchange of energy between the potential and wave kinetic energy reservoirs which is associated with the nutation of the vortex core may induce a corresponding quasi-periodic variation in the relative importance of the physical processes represented by $\mathscr{S}\hbar$, $\mathscr{S}t$, $\mathscr{H}$ and $\mathscr{D}$ in governing the evolution of three-dimensional disturbances). Unfortunately, the data needed to investigate this possibility are not presently available.

4. Discussion

We have seen by means of two-dimensional numerical simulations that nonlinear effects complicate significantly the distinction between Kelvin–Helmholtz and Holmboe instability near the KH–Holmboe transition. The 'marginal' Kelvin–Helmholtz wave exhibits two internal features which are clearly identifiable as the component modes which would form a Holmboe wave if the stratification was slightly stronger. On the other side of the KH–Holmboe transition, the component modes of the 'marginal' Holmboe wave counterpropagate until they reach sufficient amplitude to cause sustained overturning of the central temperature interface. At this point, a manifestly nonlinear phase-locking event produces a stationary vortex structure which is virtually identical to a Kelvin–Helmholtz wave.

Three-dimensional stability analyses have revealed a conspicuous absence of scale selectivity in the longitudinal secondary instabilities of both the Kelvin–Helmholtz
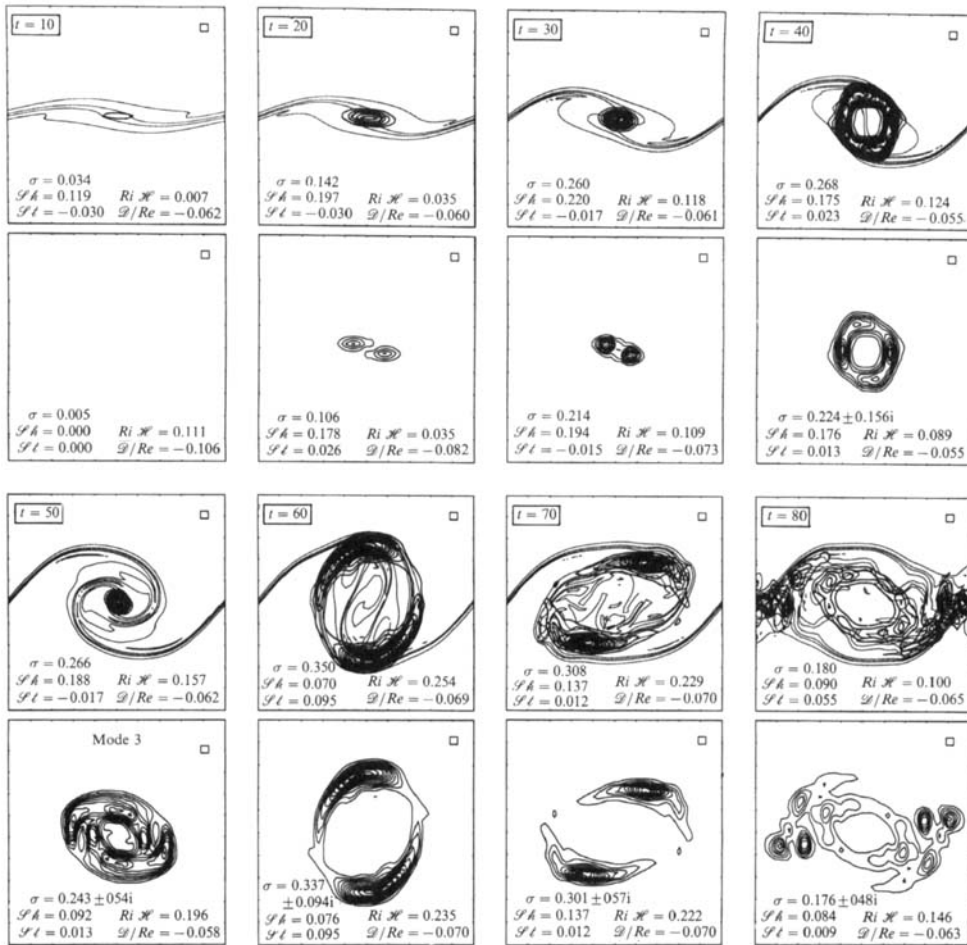
$t = 10$

$\sigma = 0.034$
$\mathcal{S}k = 0.119 \quad Ri\,\mathcal{H} = 0.007$
$\mathcal{S}\ell = -0.030 \quad \mathcal{D}/Re = -0.062$

$t = 20$

$\sigma = 0.142$
$\mathcal{S}k = 0.197 \quad Ri\,\mathcal{H} = 0.035$
$\mathcal{S}\ell = -0.030 \quad \mathcal{D}/Re = -0.060$

$t = 30$

$\sigma = 0.260$
$\mathcal{S}k = 0.220 \quad Ri\,\mathcal{H} = 0.118$
$\mathcal{S}\ell = -0.017 \quad \mathcal{D}/Re = -0.061$

$t = 40$

$\sigma = 0.268$
$\mathcal{S}k = 0.175 \quad Ri\,\mathcal{H} = 0.124$
$\mathcal{S}\ell = 0.023 \quad \mathcal{D}/Re = -0.055$

$\sigma = 0.005$
$\mathcal{S}k = 0.000 \quad Ri\,\mathcal{H} = 0.111$
$\mathcal{S}\ell = 0.000 \quad \mathcal{D}/Re = -0.106$

$\sigma = 0.106$
$\mathcal{S}k = 0.178 \quad Ri\,\mathcal{H} = 0.035$
$\mathcal{S}\ell = 0.026 \quad \mathcal{D}/Re = -0.082$

$\sigma = 0.214$
$\mathcal{S}k = 0.194 \quad Ri\,\mathcal{H} = 0.109$
$\mathcal{S}\ell = -0.015 \quad \mathcal{D}/Re = -0.073$

$\sigma = 0.224 \pm 0.156i$
$\mathcal{S}k = 0.176 \quad Ri\,\mathcal{H} = 0.089$
$\mathcal{S}\ell = 0.013 \quad \mathcal{D}/Re = -0.055$

$t = 50$

$\sigma = 0.266$
$\mathcal{S}k = 0.188 \quad Ri\,\mathcal{H} = 0.157$
$\mathcal{S}\ell = -0.017 \quad \mathcal{D}/Re = -0.062$

$t = 60$

$\sigma = 0.350$
$\mathcal{S}k = 0.070 \quad Ri\,\mathcal{H} = 0.254$
$\mathcal{S}\ell = 0.095 \quad \mathcal{D}/Re = -0.069$

$t = 70$

$\sigma = 0.308$
$\mathcal{S}k = 0.137 \quad Ri\,\mathcal{H} = 0.229$
$\mathcal{S}\ell = 0.012 \quad \mathcal{D}/Re = -0.070$

$t = 80$

$\sigma = 0.180$
$\mathcal{S}k = 0.090 \quad Ri\,\mathcal{H} = 0.100$
$\mathcal{S}\ell = 0.055 \quad \mathcal{D}/Re = -0.065$

Mode 3

$\sigma = 0.243 \pm 054i$
$\mathcal{S}k = 0.092 \quad Ri\,\mathcal{H} = 0.196$
$\mathcal{S}\ell = 0.013 \quad \mathcal{D}/Re = -0.058$

$\sigma = 0.337$
$\pm 0.094i$
$\mathcal{S}k = 0.076 \quad Ri\,\mathcal{H} = 0.235$
$\mathcal{S}\ell = 0.095 \quad \mathcal{D}/Re = -0.070$

$\sigma = 0.301 \pm 057i$
$\mathcal{S}k = 0.137 \quad Ri\,\mathcal{H} = 0.222$
$\mathcal{S}\ell = 0.012 \quad \mathcal{D}/Re = -0.070$

$\sigma = 0.176 \pm 048i$
$\mathcal{S}k = 0.084 \quad Ri\,\mathcal{H} = 0.146$
$\mathcal{S}\ell = 0.009 \quad \mathcal{D}/Re = -0.063$

FIGURE 16. Contours of $\dot{K}'(x, z)$ (solid contours) and $\tilde{\theta}(x, z)$ (dotted contours) for three-dimensional disturbances at selected times during the $Ri = 0.23$ simulation.

and the Holmboe waves near the KH–Holmboe transition. The laboratory experiments of Maxworthy & Browand (1975) yielded Holmboe wave-like structures which were distinctly three-dimensional by the time they reached visible amplitude. The spanwise variations in these waves indicated a well-defined wavelength which was similar in magnitude to the streamwise wavelength. (The three-dimensional structure of these waves is revealed more clearly in a videotape of the experiments which has been kindly provided to us by F. K. Browand.) While these observations are strongly suggestive of the three-dimensional primary Holmboe wave whose existence was demonstrated theoretically by Smyth & Peltier (1990), it could not be stated with certainty before now that the waves observed by Maxworthy & Browand (1975) were not a manifestation of secondary instability. However, it is easily seen upon inspection of figures 9(a) and 9(b) that Holmboe waves in a fluid with $Pr \gg 1$ and Re too large to permit three-dimensional primary instability show no evidence of scale-selective secondary instability, particularly not in the regime of unit horizontal aspect ratio ($b \approx \alpha = 0.3$). We thus conclude that the experiments of Maxworthy & Browand (1975) were performed at sufficiently low Reynolds number to yield three-dimensional primary instability.
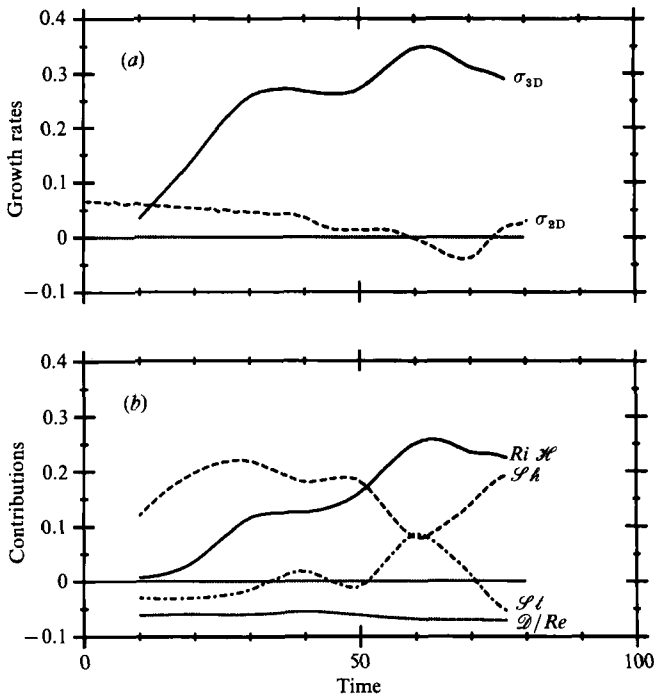
14

FIGURE 17. (a) Growth rates of ——, the dominant three-dimensional normal mode and – – –, the two-dimensional wave for the $Ri = 0.23$ simulation. (b) Contributions to σ_{3D} appearing on the right-hand side of (19).

Through detailed examinations of the spatial structures of the unstable modes of the Holmboe wave, we have learned that secondary instability is intimately associated with the plumes of the wave, and is most intense during the phase of the oscillation cycle in which the plumes are largest, particularly if the central temperature interface is overturned. In this part of the cycle, instability is driven primarily by a mixture of convective activity and the influence of the shearing deformation in the two-dimensional wave. At other points in the cycle, secondary convective activity subsides and the remaining instability is driven primarily by shear. In the laboratory experiments of Browand & Winant (1973) and Koop (1976), Holmboe waves were observed which were essentially two-dimensional except for turbulent 'puffs' which appeared at the tips of the plumes. These observations are in excellent accord with the predicted characteristics of the non-scale-selective secondary instability which we have discussed in this paper.

The Holmboe waves observed by Browand & Winant (1973) are of particular interest because they appeared after the flow had evolved through a phase in which strong Kelvin–Helmholtz instability was present. This observation substantiates our earlier contention (see §1) that the action of diffusion on a high-Prandtl-number fluid, in spite of (or perhaps aided by) the temporary appearance of Kelvin–Helmholtz instability, tends to drive the flow towards a state characterized by Holmboe instability. We thus suggest that Holmboe waves should be a common feature of mixing layers occurring in the Earth's oceans, and may in fact account for a substantial amount of mixing in regions of the ocean interior which have previously been assumed to be stable in consequence of large values of the Richardson number.

In the analysis of Kelvin–Helmholtz waves, we have found secondary stability

characteristics which are similar to those obtained by Klaassen & Peltier (1985*a*, *b*, 1991) for the case $R = 1$, $Pr = 1$, with the exception that the scale selectivity which was observed in those analyses is not evident in the present results. The validity of Klaassen & Peltier's results has been substantiated in the laboratory experiments of Thorpe (1985), in which the scale ratio R was in the range 1–1.7 and Pr had a value of 800. These experiments revealed scale-selective longitudinal instabilities in accordance with the predictions of Klaassen & Peltier (1985*b*, *c*), despite the large Prandtl number of the working fluid. It is thus apparent that the absence of scale selectivity in the results of the present analyses is due not only to the large value we have employed for the Prandtl number ($Pr = 9$) and the intense temperature gradients which the model flow can sustain as a result, but also to the sharp temperature gradient which is present in our initial conditions ($R = 3$).

In a future publication, we shall discuss transverse instabilities of KH and Holmboe waves, in particular the subharmonic instabilities which play a crucial role in the evolution of weakly stratified shear layers. The experimental results of Lawrence *et al.* (1987), suggest that the Holmboe wave may exhibit a non-orbital pairing instability, whereas our own preliminary results indicate that subharmonic instability is suppressed in these strongly stratified flows.

Future research must also focus upon the evolution of stratified shear layers in which the stratified layer and/or the horizontal boundaries are located asymmetrically with respect to the centre of the shear layer, as some degree of asymmetry is invariably present in naturally-occurring flows.

Appendix

The following are explicit expressions for the four-dimensional coefficient arrays which appear in (18):

$$\langle UU \rangle^{\lambda\nu}_{\kappa\mu} = \frac{-iB_\lambda \langle F^*_{\kappa\mu} \tilde{U} F_{\lambda\nu}\rangle}{1+\delta_{\mu 0}} + \frac{D_\nu \langle F^*_{\kappa\mu} \tilde{W} G_{\lambda\nu}\rangle}{1+\delta_{\mu 0}} - \frac{\langle F^*_{\kappa\mu} \tilde{U}_x F_{\lambda\nu}\rangle}{1+\delta_{\mu 0}} - Re^{-1}\delta_{\kappa\lambda}\delta_{\mu\nu}A_{\lambda\nu}$$
$$+ \frac{2B_\kappa B_\lambda \langle F^*_{\kappa\mu} \tilde{U}_x F_{\lambda\nu}\rangle}{A_{\kappa\mu}(1+\delta_{\mu 0})} + \frac{2iB_\kappa D_\nu \langle F^*_{\kappa\mu} \tilde{W}_x G_{\lambda\nu}\rangle}{A_{\kappa\mu}(1+\delta_{\mu 0})},$$

$$\langle UW \rangle^{\lambda\nu}_{\kappa\mu} = \frac{-\langle F^*_{\kappa\mu} \tilde{U}_z G_{\lambda\nu}\rangle}{1+\delta_{\mu 0}} + \frac{2B_\kappa B_\lambda \langle F^*_{\kappa\mu} \tilde{U}_z G_{\lambda\nu}\rangle}{A_{\kappa\mu}(1+\delta_{\mu 0})} - \frac{2iB_\kappa D_\nu \langle F^*_{\kappa\mu} \tilde{W}_z F_{\lambda\nu}\rangle}{A_{\kappa\mu}(1+\delta_{\mu 0})},$$

$$\langle UT \rangle^{\lambda\nu}_{\kappa\mu} = iRi\frac{B_\kappa D_\nu}{A_{\kappa\mu}}\delta_{\kappa\lambda}\delta_{\mu\nu},$$

$$\langle WU \rangle^{\lambda\nu}_{\kappa\mu} = -\langle G^*_{\kappa\mu} \tilde{W}_x F_{\lambda\nu}\rangle + 2i\frac{D_\mu B_\lambda}{A_{\kappa\mu}}\langle F^*_{\kappa\mu} \tilde{U}_x F_{\lambda\nu}\rangle - 2\frac{D_\mu D_\nu}{A_{\kappa\mu}}\langle F^*_{\kappa\mu} \tilde{W}_x G_{\lambda\nu}\rangle,$$

$$\langle WW \rangle^{\lambda\nu}_{\kappa\mu} = -iB_\lambda \langle G^*_{\kappa\mu} \tilde{U} G_{\lambda\nu}\rangle - D_\nu \langle G^*_{\kappa\mu} \tilde{W} F_{\lambda\nu}\rangle - \langle G^*_{\kappa\mu} \tilde{W}_z G_{\lambda\nu}\rangle - Re^{-1}\delta_{\kappa\lambda}\delta_{\mu\nu}A_{\lambda\nu}$$
$$+ 2i\frac{D_\mu B_\lambda \langle F^*_{\kappa\mu} \tilde{U}_z G_{\lambda\nu}\rangle}{A_{\kappa\mu}} + 2\frac{D_\mu D_\nu \langle F^*_{\kappa\mu} \tilde{W}_z F_{\lambda\nu}\rangle}{A_{\kappa\mu}},$$

$$\langle WT \rangle^{\lambda\nu}_{\kappa\mu} = Ri\delta_{\kappa\lambda}\delta_{\mu\nu}\left(1 - \frac{D_\mu D_\nu}{A_{\kappa\mu}}\right),$$

$$\langle TU \rangle^{\lambda\nu}_{\kappa\mu} = -\langle G^*_{\kappa\mu} \tilde{\theta}_x F_{\lambda\nu}\rangle,$$

$$\langle TW \rangle^{\lambda\nu}_{\kappa\mu} = -\langle G^*_{\kappa\mu} \tilde{\theta}_z G_{\lambda\nu}\rangle,$$

$$\langle TT \rangle^{\lambda\nu}_{\kappa\mu} = -iB_\lambda \langle G^*_{\kappa\mu} \tilde{U} G_{\lambda\nu}\rangle - D_\nu \langle G^*_{\kappa\mu} \tilde{W} F_{\lambda\nu}\rangle - (RePr)^{-1}\delta_{\kappa\lambda}\delta_{\mu\nu}(1+\delta_{\mu 0})A_{\lambda\nu},$$

in which

$$B_\lambda = \lambda\alpha + b, \quad D_\nu = \nu\pi/H, \quad A_{\lambda\nu} = B_\lambda^2 + D_\nu^2 + d^2,$$

δ is the Kronecker delta and the inner product $\langle \cdot \rangle$ is defined by

$$\langle \cdot \rangle = \frac{2}{LH} \int_0^H dz \int_0^L dx \cdot .$$

REFERENCES

BROWAND, F. K. & WANG, Y. H. 1972 An experiment on the growth of small disturbances at the interface between two streams of different densities and velocities. *Proc. Intl Symp. on Stratified Flows, August 29–31, 1972, Novosibirsk, Soviet Union*, pp. 491–498.

BROWAND, F. K. & WINANT, C. D. 1973 Laboratory observations of shear instability in a stratified fluid. *Boundary-Layer Met.* **5**, 67–77.

BUSSE, F. 1981 Transition to turbulence in Rayleigh–Bénard convection. In *Hydrodynamic Instabilities and the Transition to Turbulence* (ed. H. L. Swinney & J. P. Gollub), pp. 97–137. Springer.

CLEVER, R. M. & BUSSE, F. 1974 Transition to time-dependent convection. *J. Fluid Mech.* **65**, 625–645.

COLLINS, D. A. & MASLOWE, S. A. 1988 Vortex pairing and resonant wave interactions in a stratified free shear layer. *J. Fluid Mech.* **191**, 465–480.

DI PRIMA, R. C. & SWINNEY, H. L. 1981 Instabilities and transition in flow between concentric rotating spheres. In *Hydrodynamic Instabilities and the Transition to Turbulence* (ed. H. L. Swinney & J. P. Gollub), pp. 139–180. Springer.

HAZEL, P. 1972 Numerical studies of the stability of inviscid parallel shear flows. *J. Fluid Mech.* **51**, 39–62.

HOLMBOE, J. 1962 On the behaviour of symmetric waves in stratified shear layers. *Geofys. Publ.* **24**, 67–113.

KLAASSEN, G. P. & PELTIER, W. R. 1985*a* The evolution of finite-amplitude Kelvin–Helmholtz billows in two spatial dimensions. *J. Atmos. Sci.* **42**, 1321–1339.

KLAASSEN, G. P. & PELTIER, W. R. 1985*b* The onset of turbulence in finite amplitude Kelvin–Helmholtz billows. *J. Fluid Mech.* **155**, 1–35.

KLAASSEN, G. P. & PELTIER, W. R. 1985*c* The effect of Prandtl number on the evolution and stability of Kelvin–Helmholtz billows. *Geophys. Astrophys. Fluid Dyn.* **32**, 23–60.

KLAASSEN, G. P. & PELTIER, W. R. 1989 The role of transverse secondary instabilities in the evolution of free shear layers. *J. Fluid Mech.* **202**, 367–402.

KLAASSEN, G. P. & PELTIER, W. R. 1991 The influence of stratification on secondary instability in free shear layers. *J. Fluid Mech.* **227**, 71–106.

KOOP, C. G. 1976 Instability and turbulence in a stratified shear layer. PhD thesis, University of Southern California (also published as *DDC Rep.* ADA 026634).

KOOP, C. G. & BROWAND, F. K. 1979 Instability and turbulence in a stratified fluid with shear. *J. Fluid Mech.* **93**, 135–159.

LAPRISE, R. & PELTIER, W. R. 1989 The linear stability of nonlinear mountain waves: Implications for the understanding of severe downslope windstorms. *J. Atmos. Sci.* **46**, 545–564.

LAWRENCE, G. A., BROWAND, F. K. & REDEKOPP, L. G. 1990 The stability of a sheared density interface. *Phys. Fluids* A (in press).

LAWRENCE, G. A., LASHERAS, J. C. & BROWAND, F. K. 1987 Shear instabilities in stratified flow. *Proc. of the Third Intl Symp. on Stratified Flows, February 2–5, 1987, Pasadena, California*.

MAXWORTHY, T. & BROWAND, F. K. 1975 Experiments in rotating and stratified flows: oceanographic applications. *Ann. Rev. Fluid Mech.* **7**, 273–305.

METCALFE, R. W., ORSZAG, S. A., BRACHET, M. E., MENON, S. & RILEY, J. J. 1987 Secondary instability of a temporally growing mixing layer. *J. Fluid Mech.* **184**, 207–243.

NISHIDA, S. & YOSHIDA, S. 1982 Stability of a two-layer shear flow. *Theor. Appl. Mech.* **32**, 35–45.

ORSZAG, S. A. & PATERA, A. 1980 Subcritical transition to turbulence in plane channel flows. *Phys. Rev. Lett.* **45**, 989–993.

PIERREHUMBERT, R. T. 1986 Universal short-wave instability of two-dimensional eddies in an inviscid fluid. *Phys. Rev. Lett.* **57**, 2157–2159.

PIERREHUMBERT, R. T. & WIDNALL, S. E. 1982 The two- and three-dimensional instabilities of a spatially periodic shear layer. *J. Fluid Mech.* **114**, 59–82.

RUELLE, D. & TAKENS, F. 1971 On the nature of turbulence. *Commun. Math. Phys.* **20**, 167–192; **23**, 343–344.

SMYTH, W. D., KLAASSEN, G. P. & PELTIER, W. R. 1988 Finite amplitude Holmboe waves. *Geophys. Astrophys. Fluid Dyn.* **43**, 181–222.

SMYTH, W. D. & PELTIER, W. R. 1989 The transition between Kelvin–Helmholtz and Holmboe instability: An investigation of the overreflection hypothesis. *J. Atmos. Sci.* **46**, 3698–3720.

SMYTH, W. D. & PELTIER, W. R. 1990 Three-dimensional primary instabilities of a stratified, dissipative, parallel flow. *Geophys. Astrophys. Fluid Dyn.* **52**, 249–261.

THORPE, S. A. 1968 A method of producing a shear flow in a stratified fluid. *J. Fluid Mech.* **32**, 693–704.

THORPE, S. A. 1985 Laboratory observations of secondary structures in Kelvin–Helmholtz billows and consequences for ocean mixing. *Geophys. Astrophys. Fluid Dyn.* **34**, 175–199.

THORPE, S. A. 1987 Transition phenomena and the development of turbulence in stratified fluids. *J. Geophys. Res.* **92**, 5231–5248.

YOSHIDA, S. 1977 On a mechanism for breaking interfacial waves. *Coastal Engng Japan* **20**, 7–15.